J. Fluid Mech. (1991), *vol.* 227, *pp.* 1–33
Printed in Great Britain

Two-dimensional flow of a viscous fluid in a channel with porous walls

By STEPHEN M. COX†

School of Mathematics, University of Bristol, University Walk, Bristol BS8 1TW, UK

(Received 18 September 1989 and in revised form 14 November 1990)

We consider the flow of a viscous incompressible fluid in a parallel-walled channel, driven by steady uniform suction through the porous channel walls. A similarity transformation reduces the Navier–Stokes equations to a single partial differential equation (PDE) for the stream function, with two-point boundary conditions. We discuss the bifurcations of the steady solutions first, and show how a pitchfork bifurcation is unfolded when a symmetry of the problem is broken.

Then we describe time-dependent solutions of the governing PDE, which we calculate numerically. We analyse these unsteady solutions when there is a high rate of suction through one wall, and the other wall is impermeable: there is a limit cycle composed of an explosive phase of inviscid growth, and a slow viscous decay. The inviscid phase 'almost' has a finite-time singularity. We discuss whether solutions of the governing PDE, which are exact solutions of the Navier–Stokes equations, may develop mathematical singularities in a finite time.

When the rates of suction at the two walls are equal so that the problem is symmetrical, there is an abrupt transition to chaos, a 'homoclinic explosion', in the time-dependent solutions as the Reynolds number is increased. We unfold this transition by perturbing the symmetry, and compare direct numerical integrations of the governing PDE with a recent theory for 'Lorenz-like' dynamical systems. The chaos is found to be very sensitive to symmetry breaking.

1. Introduction

In this paper we consider a similarity solution of the Navier–Stokes equations which describes the two-dimensional flow of a viscous fluid driven by suction or injection through the porous walls of a parallel-walled channel. Insistence that the flow be of similarity form allows a reduction of the Navier–Stokes equations to a single partial differential equation (PDE) for the streamfunction in one space dimension, the Proudman–Johnson equation (Proudman & Johnson 1962). This equation, which is derived in §2, is the subject of this paper. If attention is restricted to steady flows then the PDE reduces to an ordinary differential equation (ODE), which is more amenable to analysis than the PDE.

In 1953, Berman gave a series solution of the ODE valid for small values of the Reynolds number, R. He considered the symmetric problem where there is equal suction (or injection) of fluid through the two channel walls, and he assumed correspondingly that his solutions were symmetrical about the centreline of the channel. Many authors have extended Berman's symmetric series solution, for example Terrill (1964, 1965), Shrestha (1967), Robinson (1976), Skalak & Wang

---

† Present address: Sibley School of Mechanical & Aerospace Engineering, Upson Hall, Cornell University, Ithaca, NY 14853, USA.

(1978), Brady (1984), Durlofsky & Brady (1984), Zaturska, Drazin & Banks (1988), Watson *et al.* (1990). In fact, as Zaturska *et al.* have shown, there are also asymmetric solutions of the symmetric problem.

The asymmetric steady problem, where the rates of suction at the two channel walls are not equal, was first analysed by Proudman (1960), and later by Terrill and Shrestha (Terrill & Shrestha 1965; Terrill 1967; Shrestha & Terrill 1968). They continued the *symmetric* solutions of the symmetric problem to give corresponding solutions of the asymmetric problem. In §3 we continue the *asymmetric* solutions of the symmetric problem to give new solutions of the asymmetric problem. These new solutions are calculated numerically – in detail by integrating an ODE with two-point boundary conditions – and in some cases the asymptotic form of the solution for large wall-suction rates may be inferred from the numerical solutions. Where this has been feasible we describe the results, but with little detail, of our matched asymptotics calculations.

The asymmetric solutions of the symmetric problem arise at a pitchfork bifurcation, where the symmetric solution loses stability. Bifurcation theory tells us qualitatively how this pitchfork bifurcation is unfolded when the symmetry of the problem is broken. Our numerical integrations of the ODE give quantitative details.

A particular case is examined first, in §3, when there is suction or injection at only one wall, and the other wall is impermeable. (This is the most extreme case we consider. We do not in this paper consider flows driven by suction at one wall and injection at the other, although this suction/injection problem would be interesting (Proudman 1960).) Our numerical integrations indicate that there is hysteresis, that is, a range of suction rates for which there are multiple steady solutions. They also suggest the asymptotic form of the solutions at large wall-suction or injection rates. Elsewhere (Cox 1989, 1991) we have shown analytically that the solutions we find numerically for this extreme case are the only solutions. This is not true when there is suction at both walls, and there may be a large, perhaps infinite, number of solutions.

When both walls are permeable the Berman problem has two dimensionless parameters. These may be chosen in many ways: we discuss two of these choices. In the first, a Reynolds number, R, is based on the average rate of suction (or injection) through the two channel walls, and a symmetry parameter, ϵ, is effectively the ratio of wall-suction rates. For most of our work we take ϵ to be fixed and consider the effect of varying R, that is, we consider the bifurcations along fixed-ϵ cross-sections in parameter space so that the ratio of the suction rates at the two walls is fixed. The second definition of the parameters takes a Reynolds number, $\hat{R}$, to be based on the fluid suction rate at, say, the lower wall and a second parameter, γ, to be the ratio of wall-suction rates. Fixing the Reynolds number $\hat{R}$ and varying γ then corresponds to looking at the bifurcations as the suction rate at the upper wall is varied, with that at the lower wall fixed. We show in §3.4 how the bifurcation diagrams on fixed-$\hat{R}$ cross-sections of parameter space can be derived directly from those on fixed-ϵ cross-sections with no further numerical work.

In §4 we begin our study of time-dependent solutions of the Proudman–Johnson equation. First we integrate the PDE numerically for the extreme case where there is suction at only the upper wall. When the suction rate is large, we find that there is a stable periodic solution to which all other solutions are attracted at large times. This limit cycle is composed of two parts: an explosive phase of inviscid growth, and a much slower viscous decay. Our numerical results suggest analytical forms for the solution during each of these phases which are valid in the limit as the suction rate becomes infinite. The explosive phase proves increasingly hard to calculate numerically as R (i.e. the rate of suction through the upper wall) is increased: if the spatial grid is too coarse then a numerical overflow occurs in a finite time. This overflow is removed if the spatial grid is made finer, and does not seem to correspond to a mathematical singularity in solutions of the PDE – the exact solution remains finite and continues around the limit cycle indefinitely. A similar explosive phase has been reported for flow in a channel with two impermeable walls by Childress *et al.* (1989). They observed blow-up of their numerical solution when the viscosity of the fluid was small (i.e. the Reynolds number large), and interpreted this as evidence of a mathematical singularity in solutions of the Proudman–Johnson PDE itself. In fact, further numerical work by ourselves, and Ierley (S. Childress, personal communication) indicates that their numerical blow-up, like ours, is a spurious numerical artifact which can be avoided by taking a sufficiently fine grid. However, we are unable to prove that solutions of the Proudman–Johnson equation (with prescribed boundary conditions) must remain bounded for all time, as has been proved for other dissipative PDEs, the Kuramoto–Sivashinsky equation for example (Foias *et al.* 1988). The possibility remains open that for larger R than those investigated numerically, or for different boundary conditions, solutions of the Proudman–Johnson equation may develop singularities in a finite time. We discuss this point in §5.

Zaturska *et al.* (1988) showed that for the symmetric problem (with equal rates of suction at the two channel walls) the time-dependent solutions of the Proudman–Johnson equation make a complicated transition from periodicity, through apparent quasi-periodicity, to chaos, which arises abruptly from a 'homoclinic explosion'. They made an analogy with Lorenz' system of three ODEs (Lorenz 1963) where, as for the Berman problem, symmetry is crucial to the abruptness of the transition to chaos. We pursue this analogy. We compare, in §6, some numerical integrations of the Proudman–Johnson equation for slightly asymmetric suction at the channel walls with some results from the theory of dynamical systems (Glendinning 1987) concerning asymmetric perturbations to 'Lorenz-like' systems, to find how sensitive the chaos is to symmetry breaking. Thus we investigate the effect of symmetry breaking on the transition to chaos in the same way as we investigate its effect on the steady solutions near the pitchfork bifurcation. That is, in the latter case bifurcation theory gives qualitative information and numerical integration provides quantitative details; in the former it is the theory of dynamical systems which provides the qualitative information. Matching up the qualitative and quantitative results produces no surprises near the pitchfork bifurcation in the steady problem. For the time-dependent problem, however, this matching up is not so straightforward because the region in parameter space where there are chaotic solutions turns out to be very small. In fact this surprising result can also occur in an asymmetric perturbation of the Lorenz system itself (Cox 1989, 1990). The understanding of how chaos arises when the symmetry of the problem is broken is not only of mathematical interest but also relevant to laboratory experiments, which will certainly by asymmetric (if only unintentionally).

The flows described here have numerous applications, for example for control of boundary-layer separation with suction or injection. We consider briefly the practical utility of the similarity solutions in §7: to determine this, a careful laboratory experiment should be performed. Indeed, a strong practical motivation for studying the Berman problem with one porous and one impermeable wall (§§3.1, 3.2, 4) is that the flow in such a laboratory experiment could be visualized more easily through a transparent impermeable wall than in the case which has previously received most attention, where there is suction through both walls, and experimental apparatus would simply obscure the view.

2. The Berman problem

The Berman problem is as follows. There is two-dimensional flow in a channel $-\infty < x < \infty$, $-h < y < h$. The fluid is incompressible, so we may introduce a stream function $\Psi(x, y, t)$, in terms of which $u = \partial\Psi/\partial y$ and $v = -\partial\Psi/\partial x$, where u is the velocity component along the channel and v the velocity component across the channel. The Navier–Stokes equations then reduce to the vorticity equation,

$$\frac{\partial}{\partial t}\nabla^2\Psi + \frac{\partial(\nabla^2\Psi, \Psi)}{\partial(x, y)} = \nu\nabla^4\Psi, \tag{1}$$

where ν is the kinematic viscosity of the fluid. The boundary conditions are no slip at the walls and constant uniform suction, $v = V_1$, at the upper wall, and $v = -V_{-1}$ at the lower wall, that is

$$\left.\begin{aligned} u = 0, \quad v = V_1 \quad &\text{at} \quad y = h \\ u = 0, \quad v = -V_{-1} \quad &\text{at} \quad y = -h \end{aligned}\right\}. \tag{2}$$

Non-dimensionalizing x and y by h, u and v by $\frac{1}{2}(V_1 + V_{-1})$ (which is non-zero because we only consider the case where V_1 and V_{-1} have the same sign), t by $2h/(V_1 + V_{-1})$, and Ψ by $\frac{1}{2}h(V_1 + V_{-1})$, we obtain

$$\frac{\partial}{\partial t}\nabla^2\Psi + \frac{\partial(\nabla^2\Psi, \Psi)}{\partial(x, y)} = R^{-1}\nabla^4\Psi, \tag{3}$$

where $R = (V_1 + V_{-1})\,h/2\nu$ is the Reynolds number. The boundary conditions for Ψ are

$$\left.\begin{aligned} \Psi = -1-\epsilon, \quad \Psi_y = 0 \quad &\text{at} \quad y = 1 \\ \Psi = 1-\epsilon, \quad \Psi_y = 0 \quad &\text{at} \quad y = -1 \end{aligned}\right\}, \tag{4}$$

where $\epsilon = (V_1 - V_{-1})/(V_1 + V_{-1})$. The special case $\epsilon = 0$, which corresponds to equal rates of suction through upper and lower walls, is the symmetric case which has previously been considered by many authors. Another special case, $\epsilon = 1$, corresponds to flow in a channel with a porous upper wall and an impermeable lower wall.

There is a similarity solution to (3), (4) of the form

$$\Psi(x, y, t) = xf(y, t), \tag{5}$$

and in terms of $f(y, t)$ the vorticity equation becomes the Proudman–Johnson equation,

$$f_{yyt} = R^{-1}f_{yyyy} + ff_{yyy} - f_y f_{yy} \tag{6}$$

with boundary conditions

$$\left.\begin{aligned} f(1, t) = -1-\epsilon, \quad &f_y(1, t) = 0 \\ f(-1, t) = 1-\epsilon, \quad &f_y(-1, t) = 0 \end{aligned}\right\}. \tag{7}$$

(Proudman & Johnson 1962 give an integrated form of (6).)

Note that when V_1 and V_{-1} have the same sign, $R > 0$ corresponds to suction through each wall and $R < 0$ to injection. In the latter case, our non-dimensionalization reverses the direction of time. Note also that the Reynolds number is defined with respect to the average rate of suction through the upper and lower walls. It may seem more natural to fix the suction velocity at one wall, and to define a Reynolds number with respect to that velocity, for example if we wish to examine the bifurcations as the rate of suction at the other wall is varied. We consider this in §3.

As noted by Berman (1953) for the symmetric case $\epsilon = 0$, there are steady solutions $F(y)$ which satisfy

$$F^{\mathrm{iv}} + R(FF''' - F'F'') = 0 \tag{8}$$

with boundary conditions

$$\left.\begin{aligned} F(1) &= -1-\epsilon, & F'(1) &= 0 \\ F(-1) &= 1-\epsilon, & F'(-1) &= 0 \end{aligned}\right\}. \tag{9}$$

For convenience, particularly in our numerical work, we often work with the first integral of (8),

$$F''' + R(FF'' - F'^2) + \beta = 0, \tag{10}$$

where β, the constant of integration, is a pressure coefficient – that is, the pressure, non-dimensionalized with $\rho(V_1 + V_{-1})^2$, is $p = p_0(y) - \frac{1}{2}\beta x^2/R$.

Terrill & Shrestha (1964, 1965), have given a series solution for $F(y)$ which is valid for small R. In our notation this is

$$F(y) = F_0(y) + RF_1(y) + R^2F_2(y) + \dots \quad \text{as} \quad R \to 0, \tag{11}$$

where
$$F_0(y) = \tfrac{1}{2}y(y^2-3) - \epsilon, \tag{12}$$

and
$$F_1(y) = \tfrac{1}{280}y(y^6 - 3y^2 + 2) + \tfrac{1}{8}\epsilon(y^4 - 2y^2 + 1). \tag{13}$$

We have used this small-R expansion as a starting point for, and as a check on, our numerical integrations.

We shall discuss in later sections the temporal stability of the steady solutions $F(y)$ to disturbances of the similarity form (5). We determine this stability by the method of normal modes: we consider disturbances of the form $f(y,t) = F(y) + g(y,t) = F(y) + e^{\lambda t}G(y)$ where g is small. Then the solution F is stable if the real part of $R\lambda$ is negative for all modes. By linearization of (6) we obtain the equation for G,

$$G^{\mathrm{iv}} + R(FG''' - F'G'' - F''G' + F'''G) = R\lambda G''. \tag{14}$$

The boundary conditions on G are that G and G' vanish at the walls $y = \pm 1$. This eigenvalue problem has a discrete spectrum, and two families of eigenmodes have been identified by Zaturska *et al.* (1988), named $q_1, q_2, \dots$ and $r_1, r_2, \dots$. By solving the eigenproblem for G (numerically) we can find and classify the bifurcations of the steady solutions $F(y)$ (Zaturska *et al.* 1988; Watson *et al.* 1990).

3. Steady solutions: numerical and asymptotic results

We use shooting to find numerical solutions of the two-point boundary-value problems for $F(y)$ and its eigenmodes $G(y)$. A careful choice of the direction of integration across the channel is often necessary to ensure that we integrate in the more efficient sense through the boundary layers which arise near the walls. Numerical difficulties arise at large $|R|$, due either to a failure of the integration routine (the solution blows up in mid-channel) or a failure of the shooting to converge.

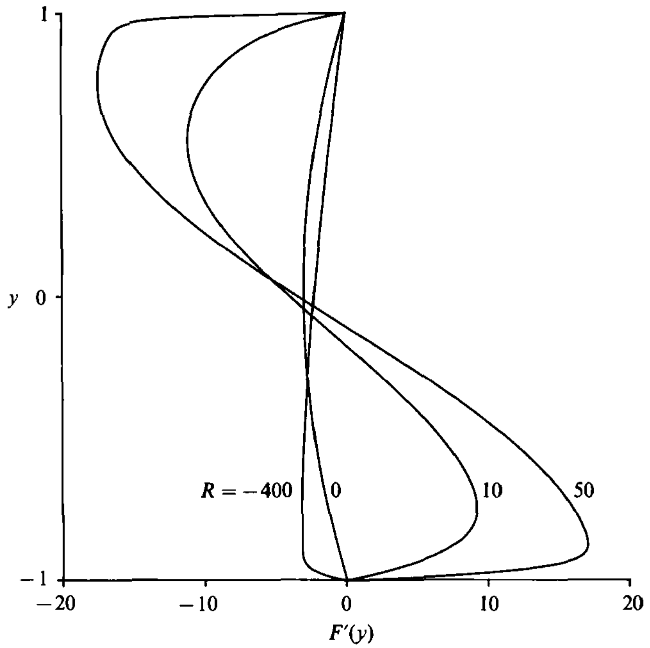

FIGURE 1. Velocity profiles, $F'(y)$ against y, for $R = -400, 0, 10, 50$ when $\epsilon = 1$.

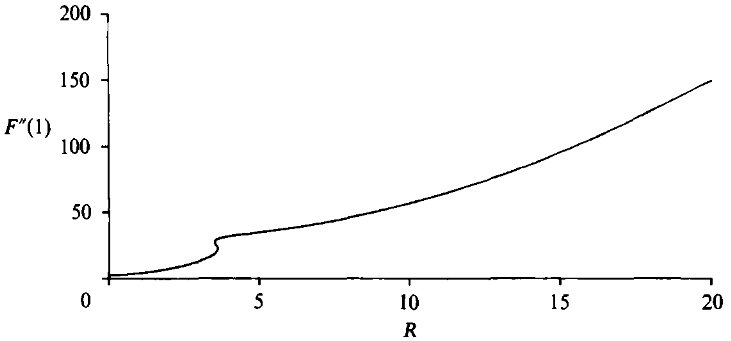

FIGURE 2. $F'''(1)$ against R, for $R > 0$ when $\epsilon = 1$. This is the only branch of steady solutions to (8), (9) when $\epsilon = 1$ (Cox 1991). Note the small interval of hysteresis for $R \approx 3.6$. ($F'''(1)$ is proportional to the skin friction at the upper wall.)

To solve the time-dependent problem (6) and (7) numerically we use a general package (Berzins & Dew 1989) designed to integrate elliptic-parabolic systems of PDEs by the method of lines. The initial condition $f(y, 0) = f_0(y)$ is decided by the context of the integration. We have taken care that sufficiently many polynomials are used in the semi-discretization to adequately resolve, for example, the boundary layers near the channel walls. Otherwise plausible, but spurious numerical solutions can be found (see §4).

3.1. *Numerical results for* $\epsilon = 1$

We have numerically continued for increasing $|R|$ the unique small-R branch of solutions which is given by the series (11). These numerical results are summarized in the following figures: figure 1 shows velocity profiles for some of the flows; figure 2 shows a typical state variable, $F'''(1)$, plotted against R for $R > 0$ (the quantity

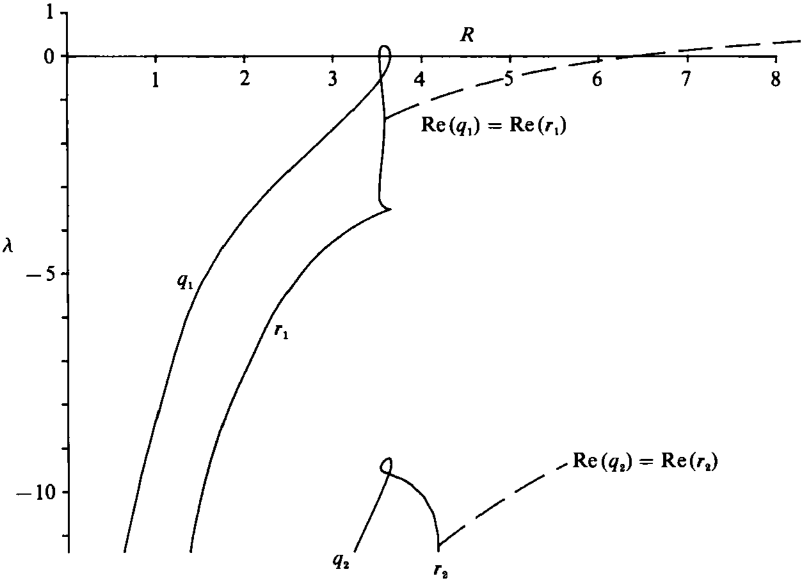

FIGURE 3. Eigenvalues of the linear stability problem (14) for the basic flow $F(y)$, plotted against R when $\epsilon = 1$. The first four eigenvalues shown are: q_1, r_1, q_2, r_2. Solid lines represent real eigenvalues, and dashed lines the real parts of eigenvalues with non-zero imaginary parts. The intersections of the q_1-loop with the R-axis mark the interval of hysteresis. The Hopf bifurcation occurs when $\mathrm{Re}(q_1) = \mathrm{Re}(r_1)$ becomes positive at $R \approx 6.3775625$.

$F''(1)$ is proportional to the skin friction, $\mu \partial u/\partial y$, at the upper wall); figure 3 shows the eigenvalues q_1, r_1, q_2, r_2 of the basic flow, $F(y)$.

When $R \approx 3.27977$, the skin friction at the lower wall vanishes (that is, $F''(-1) = 0$) and for greater values of the Reynolds number there is backflow in the lower part of the channel. When $R \approx 3.654149$ there is a turning point (saddle-node bifurcation) where the eigenvalue q_1 passes through zero and the solution branch loses stability. We may track round onto the branch of unstable solutions for $R < 3.654149$ until $R \approx 3.525373$, where q_1 again passes through zero and there is a second turning point, where the solution branch regains stability (see figures 2 and 3). Thus (3.525373, 3.654149) is an interval of hysteresis where there are three co-existing steady solutions – two stable and one unstable. At $R \approx 3.58875$ the eigenvalues q_1 and r_1 coalesce and become a complex-conjugate pair with negative real part; at $R \approx 4.175$, q_2 and r_2 do likewise, and at $R \approx 5$, q_3 and r_3 do so too. When R reaches 6.3775625 the real part of $q_1 = r_1^*$ passes through zero and the steady solution loses stability in a supercritical Hopf bifurcation. The steady solution remains unstable as $R \rightarrow \infty$. (We have not calculated $q_{2,3}$ or $r_{2,3}$ for large R, so we do not know whether the real parts of these eigenvalues become positive as R is increased, that is, whether there are further Hopf bifurcations of the steady solution for $R > 6.3775625$.) For all negative values of the Reynolds number we find a single solution, and this solution is stable. Elsewhere (Cox 1989, 1991) we have shown analytically that there are no other steady solutions than those described above.

3.2. *Asymptotic solution for* $\epsilon = 1$ *as* $R \rightarrow -\infty$

Our numerical integrations suggest the following asymptotic form for the solution $F(y)$ in the limit as $R \rightarrow -\infty$. (We have been unable to identify from our integrations the asymptotic form of the solution in the limit as $R \rightarrow +\infty$.)

Away from the lower wall $y = -1$ there is an inviscid outer solution which we denote by $\Phi(y, \rho)$, where $\rho = -R$. This outer solution can be expanded as a power series in $\rho^{-\frac{1}{2}}$,

$$\Phi(y,\rho) = -2\cos\left(\tfrac{1}{4}\pi\,(y-1)\right) + \tfrac{1}{2}\rho^{-\frac{1}{2}}k(y-1)\sin\left(\tfrac{1}{4}\pi\,(y-1)\right) + O(\rho^{-1}) \quad \text{as} \quad \rho \to \infty, \tag{15}$$

that is, as $R \to -\infty$, for fixed $y \neq -1$, where $k \approx 0.812022$. The constant k arises from matching Φ with the boundary-layer solution which holds near the lower wall, and it is $(\frac{1}{2}\pi)^{\frac{1}{2}} Y_0$, where $p(Y) \sim Y - Y_0$ as $Y \to \infty$ and $p(Y)$ is the Falkner–Skan solution for $m = 1$. Here m is the conventional notation for the parameter (see Batchelor 1967, p. 316). The viscous boundary layer, the inner solution near the lower wall, is to leading order the well-known Falkner–Skan profile

$$F(y) = \theta(\eta, \rho) = \rho^{-\frac{1}{2}}\{-(\tfrac{1}{2}\pi)^{\frac{1}{2}} p((\tfrac{1}{2}\pi)^{\frac{1}{2}}\eta) + O(\rho^{-\frac{1}{2}})\} \quad \text{as} \quad \rho \to \infty, \tag{16}$$

where $\eta = \rho^{\frac{1}{2}}(y+1)$ is the stretched boundary-layer variable.

These asymptotic results are in excellent agreement with our numerical results. For example from the expressions above we find that

$$F''(1) = \tfrac{1}{8}\pi^2 + \tfrac{1}{2}(\tfrac{1}{2}\pi)^{\frac{3}{2}} Y_0 \rho^{-\frac{1}{2}} + O(\rho^{-1}), \tag{17}$$

$$F''(-1) = -(\tfrac{1}{2}\pi)^{\frac{3}{2}} p''(0)\rho^{\frac{1}{2}} + O(1), \tag{18}$$

$$\beta = -\tfrac{1}{4}\pi^2\rho - \tfrac{1}{2}\pi k \rho^{\frac{1}{2}} + O(1) \quad \text{as} \quad \rho \to \infty. \tag{19}$$

At $R = -400$ these give $\rho^{-\frac{1}{2}}F''(-1)$, $F''(1)$ and $\rho^{-1}\beta$ to be -2.427, 1.265, -2.531 respectively. Our numerical results for these quantities are -2.474, 1.267, -2.533. These (and other) numerical results suggest that the terms of order 1 in (18) and (19) are -0.95 and -0.8 respectively.

3.3. *Numerical results for* $0 < \epsilon < 1$

We have described above the solutions of the steady Berman problem (8), (9) when $\epsilon = 1$, that is, when there is suction at only the upper wall. We now describe our numerical results for the values of ϵ which bridge that case and the more extensively studied symmetric problem, where $\epsilon = 0$. Our numerical integrations have been for the examples of $\epsilon = \frac{1}{19}, \frac{1}{3}, \frac{2}{3}, \frac{9}{11}$, for as large a range of R as has been feasible. Some results for general ϵ are already known (Terrill 1967; Terrill & Shrestha 1965; Shrestha & Terrill 1968), and we summarize them in our notation for completeness, while devoting more detail to our new results.

In order to put the results for $0 < \epsilon < 1$ into context, we briefly review some of the solutions which are known when $\epsilon = 0$. Robinson (1976) has described the symmetric steady solutions of (8), (9) when $\epsilon = 0$: there is a single-valued branch of solutions (called solutions of type *I*) which exists for all $R \in \mathbb{R}$, and a distinct pair of solutions (of types *II* and *III*) which arise from a turning-point bifurcation at $R = R_3 \approx 12.165$. Zaturska *et al.* (1988) have investigated the stability of these solutions: those of type *I* are stable for $R < R_1 \approx 6.001353$ and unstable for $R > R_1$, losing stability in a pitchfork bifurcation where two stable asymmetric solutions (of types I_1 and I_1') are born. The asymmetric solutions lose stability at $R = R_{11} \approx 12.963$ in supercritical Hopf bifurcations (where they each throw off a time-periodic solution of the PDE (6)). They remain unstable for all $R > R_{11}$. The symmetric solutions of type *II* and type *III* are unstable for all $R > R_3$, and at least one further pair of asymmetric solutions is shed in a pitchfork bifurcation (from the type *III* branch) at $R_4 \approx 15.4146$.

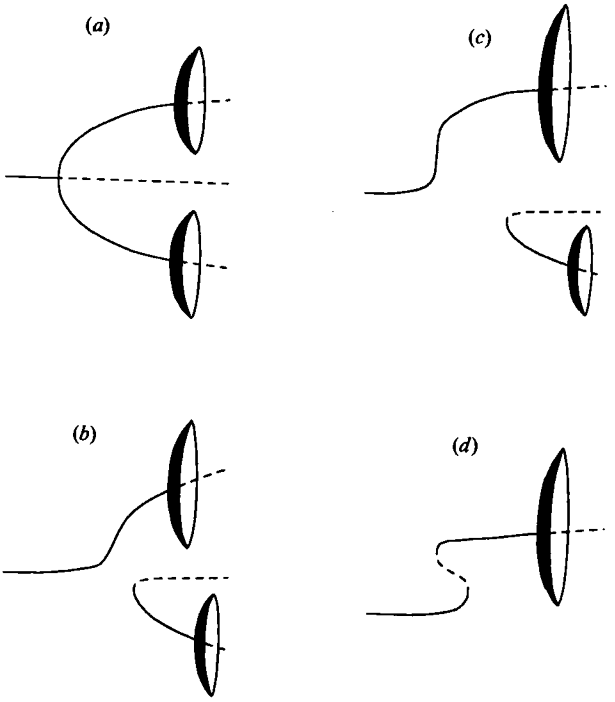

FIGURE 4. Bifurcation diagrams, F against R, for (a) $\epsilon = 0$; (b) $0 < \epsilon < \epsilon_1$; (c) $\epsilon = \epsilon_1 \approx 0.86$, and (d) $\epsilon = 1$. Solid lines represent stable solutions, dashed lines unstable solutions, and the shading represents the time-dependent solutions of the Proudman–Johnson PDE (6) which are shed at supercritical Hopf bifurcations.

We have integrated (10), (9) on the solution branches which are continuations into $\epsilon \neq 0$ of the solutions of types I, I_1, I_1' to the symmetric problem, when $\epsilon = 0$. We have not followed the solutions of types *II* and *III* into $\epsilon \neq 0$ because our results for the symmetric problem suggest that they will be unstable, and will play no important role in the time-dependent problem. We note, however, that a steady solution being unstable does not necessarily mean that it is unimportant in the time-dependent problem. Indeed, in §6 we show how the unstable steady solution of type *I* governs the dynamics of the unsteady problem.

The bifurcation diagrams of F against R are shown in figure 4 for fixed $0 \leqslant \epsilon \leqslant 1$: their qualitative features are based on our numerical results and are discussed below. (Recall that we have considered only suction/suction or injection/injection at the walls, that is, $|\epsilon| \leqslant 1$.)

When $\epsilon = 0$, there is a pitchfork bifurcation followed by a pair of Hopf bifurcations on the outer prongs of this pitchfork. The pitchfork bifurcation is a result of the symmetry of the problem, that is, the invariance of (8), (9) under the transformation $F(y) \mapsto -F(-y)$. In general a pitchfork is of codimension two. Zaturska *et al.* (1988) show by a perturbation analysis how this pitchfork will be broken for $0 < \epsilon \ll 1$ (in their figure 6) and our numerical results are consistent with their analysis. The symmetry of the system when $\epsilon = 0$ implies that the two Hopf bifurcations occur at the same value of the Reynolds number (figure 4a). For $\epsilon > 0$ the pitchfork is broken and a primary branch (in these diagrams, the upper one) emerges: in a quasi-static variation of R, increasing R from zero, say, the solution always takes the upper

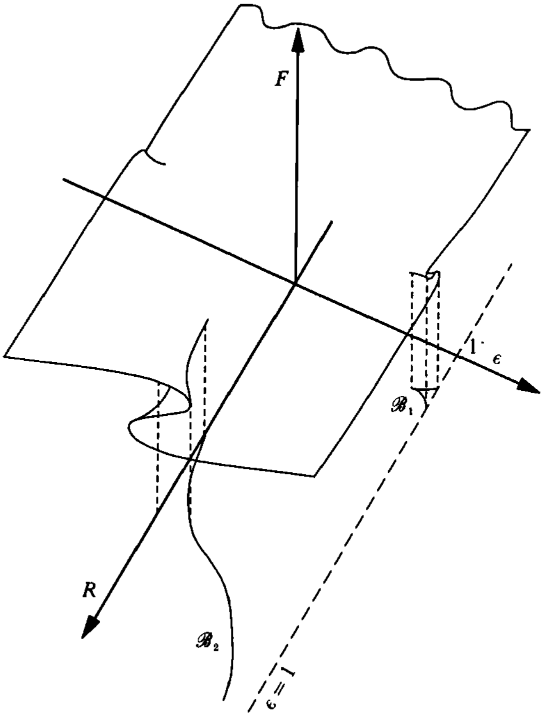

FIGURE 5. Two-parameter bifurcation diagram: F against R and ϵ. Projecting the solution surface down onto the (R, ϵ)-plane reveals the cusped regions of multiple solutions. (We have indicated this projection only for $\epsilon > 0$: $\epsilon < 0$ follows by symmetry.)

branch for $\epsilon > 0$ (figure 4*b*), whereas for $\epsilon = 0$ there is no distinguished branch. For $\epsilon > 0$ the upper branch loses stability in a Hopf bifurcation before the lower. As ϵ is increased further, the saddle-node bifurcation at which the stable/unstable pair of solutions is born occurs for larger values of R (that is, in these diagrams it moves to the right). Increasing ϵ to ϵ_1, where from our numerical results $0.85 < \epsilon_1 < 0.87$, introduces a hysteresis point into the bifurcation diagram, so that when ϵ is greater than ϵ_1 there is a range $(R_{\mathrm{tp1}}, R_{\mathrm{tp2}})$ of R for which three steady solutions exist on the primary branch (figure 4*c*). Finally, when $\epsilon = 1$ the secondary (disjoint) branches of solutions have moved out to infinity, and the only steady solutions lie on the primary branch (figure 4*d*). In what follows, we shall refer to upper, middle and lower branches of solutions – this naming of branches is with respect to these bifurcation diagrams, that is, for $0 < \epsilon < 1$ the upper branch is the primary branch, the middle and lower branches are respectively the unstable and stable branches born in the saddle-node bifurcation. The middle branch is unstable for all values of the Reynolds number for which it exists, and the upper and lower branches lose stability in Hopf bifurcations as R is increased.

We can summarize these bifurcations in a single two-parameter bifurcation diagram, of which each of the fixed-ϵ diagrams in figure 4 is a cross-section. Projecting the solution surface down onto the (R, ϵ)-plane shows for which parameters there are multiple steady solutions (see figure 5): there are three steady solutions inside the cusped regions whose boundaries are $\mathscr{B}_1$ and $\mathscr{B}_2$.

Figure 6 shows numerically calculated values for $F''(-1)$ when $\epsilon = \frac{1}{3}$ and $\epsilon = \frac{2}{3}$. (Branches of solutions which end abruptly do so when numerical difficulties prevent

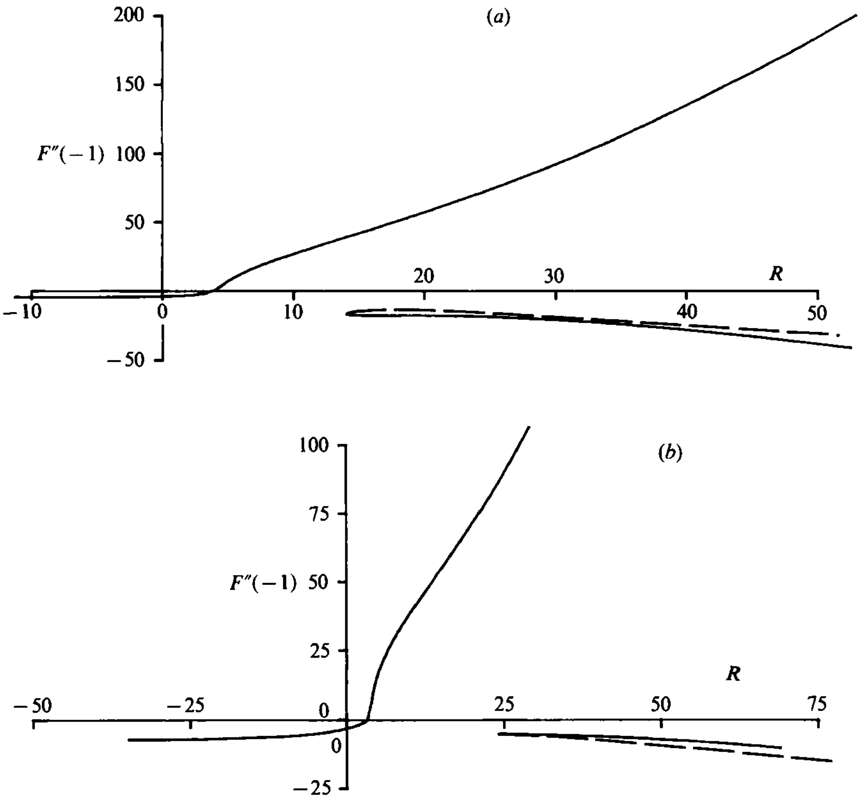

FIGURE 6. Numerical results for $F'''(-1)$ against R. Solid lines represent upper and lower branches of solutions, dashed lines the middle branch. (*a*) $\epsilon = \frac{1}{3}$ corresponds to figure 4(*b*). (*b*) $\epsilon = \frac{2}{3}$ also corresponds to figure 4(*b*), but the branches we have named as 'middle' and 'lower' for small ϵ do not now lie where their names suggest.

further integration.) Note that the graph of $F'''(-1)$ against R is qualitatively like figure 4(*b*) when $\epsilon = \frac{1}{3}$, but when $\epsilon = \frac{2}{3}$, the middle and lower branches have swapped places.

We know that the secondary (disjoint) branches exist for $\epsilon \leqslant 0.9$ because we have located them numerically. However, we also know that they do not exist for $\epsilon = 1$ (Cox 1989, 1991). It seems that they exist for all $\epsilon < 1$, but that they move out to infinity as $\epsilon \rightarrow 1-$. Also, our numerical results indicate that $R_{\mathrm{tp}} \propto (1-\epsilon)^{-1}$ as $\epsilon \rightarrow 1$, where R_{tp} is that value of the Reynolds number at which the secondary solutions are born, at the turning point (saddle-node bifurcation).

3.4. *Bifurcations for fixed suction at one wall*

The fixed-ϵ bifurcation diagrams for the steady Berman problem which we have so far presented describe the solutions as the total flow rate through the walls of the channel is varied with the *ratio* of the fluid velocities through the walls held fixed. A problem of more physical interest (and of greater experimental convenience) is with fixed suction at, say, the lower wall and variable suction at the upper wall.

Let γ be the ratio of suction rates through the two walls, $\gamma = V_1/V_{-1}$ (we consider in this subsection the case of suction, but not injection, through both walls because this is where the interesting bifurcations are). Then $R = V_{-1}h(\gamma+1)/2\nu$ and $1-\epsilon = 2/(\gamma+1)$ so that $R(1-\epsilon) = V_{-1}h/\nu = \hat{R}$ is the Reynolds number based on the suction

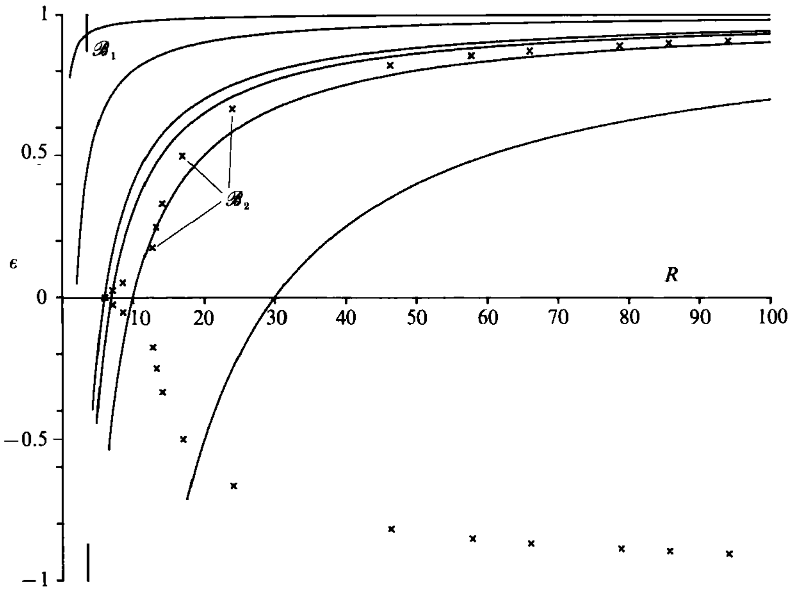

FIGURE 7. The crosses indicate the saddle-node bifurcations at which the middle and lower branches of solutions arise (determined numerically). They lie on the curve $\mathscr{B}_2$ (see figure 5). $\mathscr{B}_1$ is the boundary of the (very thin) region of hysteresis (see figures 2 and 5). The solid curves are, from top to bottom, $\hat{R} \equiv R(1-\epsilon) = \frac{1}{4}, 2, 6.0013, 7, 10, 30$.

velocity through the lower wall. Therefore as we vary V_1 with V_{-1} fixed we move along a curve $\Gamma(\hat{R})$ in (R, ϵ)-parameter space on which $\hat{R}$ is held fixed. There is a family of such curves, each parametrized by γ. The bifurcations along each curve $\Gamma(\hat{R})$ can readily be found from the (R, ϵ)-plane without further numerical work.

In figure 7, the solid lines represent the curves $\Gamma(\hat{R})$ for various values of $\hat{R}$, and the crosses indicate the saddle-node bifurcation at which the secondary branch of solutions is born as R is increased for fixed ϵ, that is, points on $\mathscr{B}_2$ determined by numerical integration (figure 5). Figure 8 shows fixed-$\hat{R}$ bifurcation diagrams of F, as γ is varied. For small values of $\hat{R}$ $(< \hat{R}_1)$ there is hysteresis over a small interval in γ (figure 8*a*). As $\hat{R}$ is increased the interval of hysteresis diminishes, and the limiting case where there is a single inflexion (or hysteresis) point occurs when $\Gamma(\hat{R}_1)$ passes through the cusp of $\mathscr{B}_1$. When $\hat{R}_1 < \hat{R} < \hat{R}_2 \approx 6.001353$, there is a single solution for all $\gamma > 0$ (figure 8*b*). Then an inflexion point is introduced on $\Gamma(\hat{R}_2)$, which passes through the cusp of $\mathscr{B}_2$ (figure 8*c*). For $\hat{R}_2 < \hat{R} < \hat{R}_3$ there is again hysteresis (figure 8*d*). There is a critical value of $\hat{R}$ at which a secondary branch of solutions is introduced for large γ. This value is $\hat{R}_3 \approx 9.57$, which follows from a numerical fit of our data, which shows that the saddle-node bifurcations lie on a curve given by $\hat{R} = R(1-\epsilon) = 9.57\ldots + O(1-\epsilon)$ as $\epsilon \to 1-$. As $\hat{R}$ is increased the interval of hysteresis diminishes until the curve $\mathscr{B}_2$ becomes tangent to $\Gamma(\hat{R})$, when $\hat{R} = \hat{R}_4 \approx 10.5$ (the bifurcations for $\hat{R}_3 < \hat{R} < \hat{R}_4$ are shown in figure 8*e*) and so there is a hysteresis point. For $\hat{R}_4 < \hat{R}$ there is a single-valued primary branch and a disjoint, secondary pair of solutions which exist for $\gamma > -1 + 2R_{\mathrm{tp}}/\hat{R}$ (figure 8*f*). Note that the symmetric case corresponds to $\gamma = 1$.

The viewpoint taken above, where the suction rate at the lower wall is fixed and that at the upper wall varied, results in a set of bifurcation diagrams (figure 8) which are more complicated than those (figure 4) for which the ratio of suction rates (ϵ) is

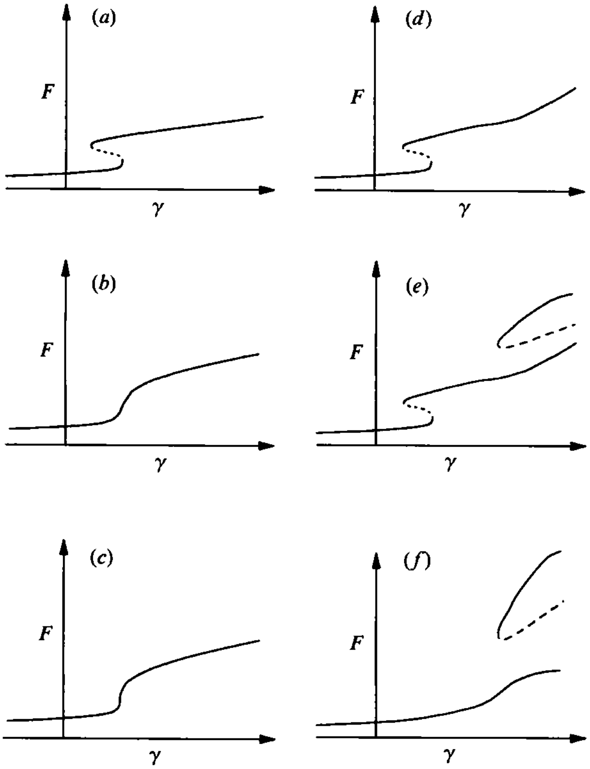

FIGURE 8. Bifurcation diagrams (F against γ) along the six curves shown in figure 7. (a) $\hat{R} = \frac{1}{4}$; (b) $\hat{R} = 2$; (c) $\hat{R} = 6.0013$; (d) $\hat{R} = 7$; (e) $\hat{R} = 10$; (f) $\hat{R} = 30$. These diagrams show the bifurcations as the suction rate at the upper wall is varied, with the suction rate at the lower wall fixed.

held fixed. The two sets of bifurcation diagrams are, of course, just different ways of taking one-dimensional sections through the solution sheet in figure 5, but the more complicated diagrams in figure 8 are the more relevant ones to a laboratory experiment.

3.5. *Asymptotic results for* $\epsilon \in (0, 1)$ *as* $R \to \pm\infty$

3.5.1. $R \to -\infty$

Proudman (1960) has described the asymptotic form of the solution for general values of ϵ as $R \to -\infty$, and we summarize his results here in our notation for completeness. There are two inviscid, sinusoidal outer solutions, Φ_+ in the upper part of the channel, and Φ_- in the lower, where the leading approximations satisfy

$$\Phi_{0\pm} = (\mp 1 - \epsilon)\cos\{\tfrac{1}{2}\pi(y \mp 1)/(1 \pm \epsilon)\}, \tag{20}$$

and these are matched at a viscous inner layer near $y = y^* = -\epsilon$. It is clear from (20) that Φ_0, Φ_0' and Φ_0'' are continuous at $y = y^*$ whereas Φ_0''' is not. In the higher-order viscous layer near $y = y^*$, F is of the form

$$F(y) = -\tfrac{1}{2}\pi(y - y^*) + \rho^{-\frac{3}{2}}\theta_0(\rho^{\frac{1}{2}}(y - y^*)) + o(\rho^{-\frac{3}{2}}), \tag{21}$$

for $|y - y^*| \ll 1$, where we denote $-R$ by ρ for convenience, and where

$$\theta_0'''(\eta) = \frac{\pi^3}{4(1-\epsilon)^2}\left(\frac{1}{2} - \frac{\epsilon}{(1+\epsilon)^2}\int_{-\infty}^{\eta} \mathrm{e}^{-\pi s^2/4}\,\mathrm{d}s\right). \tag{22}$$

(The constants of integration which are introduced when integrating (22) to find θ_0 are determined later in the asymptotic matching process.) We have found excellent agreement between Proudman's asymptotics and our numerical results. For example, (20) implies that $\Phi''_{0+}(1)/\Phi''_{0-}(-1) = -(1-\epsilon)/(1+\epsilon)$: when $\epsilon = \frac{9}{11}$, so that $-(1-\epsilon)/(1+\epsilon) = -\frac{1}{10}$, and $R = -10000$, our numerical integrations give $F''(1)/F''(-1) = -0.1000\ldots$.

In the limits as $\epsilon \to 0, 1$, Proudman's asymptotics for $\epsilon \in (0, 1)$ agree with the known asymptotic forms of the solution for those cases as $R \to -\infty$ (Zaturska *et al.* for $\epsilon = 0$; this paper for $\epsilon = 1$). That is, the limits as $\epsilon \to 0, 1$ are not singular.

3.5.2. $R \to \infty$, *middle branch*

Terrill (1967) has given the asymptotic form of the solution on the middle branch for general ϵ, assuming that there is an inviscid solution away from the walls which is linear in y, and that there is a boundary layer at each wall. In our notation, his results are

$$F(y) = \Phi(y) = \left\{-\epsilon + R^{-1}\frac{\epsilon}{1-\epsilon^2} + R^{-2}\frac{2\epsilon(5+\epsilon^2)}{(1-\epsilon^2)^3} + O(R^{-3})\right\}$$

$$+y\left\{-1 - R^{-1}\frac{1}{1-\epsilon^2} - R^{-2}\frac{4(1+2\epsilon^2)}{(1-\epsilon^2)^3} + O(R^{-3})\right\} \quad \text{as} \quad R \to \infty \qquad (23)$$

for fixed $y \in (-1, 1)$. Near the boundary layers near the walls, $F(y) = \phi_\pm(\eta_\pm)$, where

$$\phi_\pm(\eta_\pm) = (\mp 1 - \epsilon) \pm R^{-1}\left\{\eta_\pm + \frac{\exp[-(1\pm\epsilon)\eta_\pm] - 1}{1\pm\epsilon}\right\}$$

$$\pm R^{-2}\left[\left\{\frac{\eta_\pm^2}{2(1\pm\epsilon)} + \frac{3\eta_\pm}{(1\pm\epsilon)^2} + \frac{(4\mp 2\epsilon)}{(1\pm\epsilon)^3(1\mp\epsilon)}\right\}\exp\{-(1\pm\epsilon)\eta_\pm\}\right.$$

$$\left.+\left\{\frac{\eta_\pm}{(1-\epsilon^2)} - \frac{(4\mp 2\epsilon)}{(1\pm\epsilon)^3(1\mp\epsilon)}\right\}\right] + O(R^{-3}) \quad \text{as} \quad R \to \infty, \qquad (24)$$

and where $\eta_\pm = R(1 \mp y)$ near $y = \pm 1$. The pressure coefficient is then

$$\beta = R + \frac{2}{1-\epsilon^2} + \frac{(9+15\epsilon^2)}{R(1-\epsilon^2)^3} + O(R^{-2}) \quad \text{as} \quad R \to \infty. \qquad (25)$$

These expansions give good agreement with our numerical results when ϵ is small (for example $\frac{1}{19}$). For larger values of ϵ (we have taken $\epsilon = \frac{1}{3}, \frac{2}{3}, \frac{9}{11}$) the linear profile for $\Phi(y)$ seems to be replaced by a sinh profile, $F \sim R^a A \sinh B(y-C) + o(R^a)$, for some constants A, B, C, a (which depend on ϵ). We have not been able to integrate (10) numerically for sufficiently large values of R even to determine a, the power of R with which F scales as $R \to \infty$.

4. Unsteady solutions for suction at the upper wall only ($\epsilon = 1$)

So far we have described some steady solutions of the Berman problem. Now we turn to the unsteady solutions: first we consider the limit cycle which exists for large R when the lower wall is impermeable, and there is suction through the upper wall. In §6 we shall consider the route to chaos in the near-symmetric problem.

Solving (6) and (7) numerically for $\epsilon = 1$ we find that the only stable solution for $R < R_{\mathrm{Hopf}} \approx 6.3775625$ is the steady solution which we have described in §3.1 – this

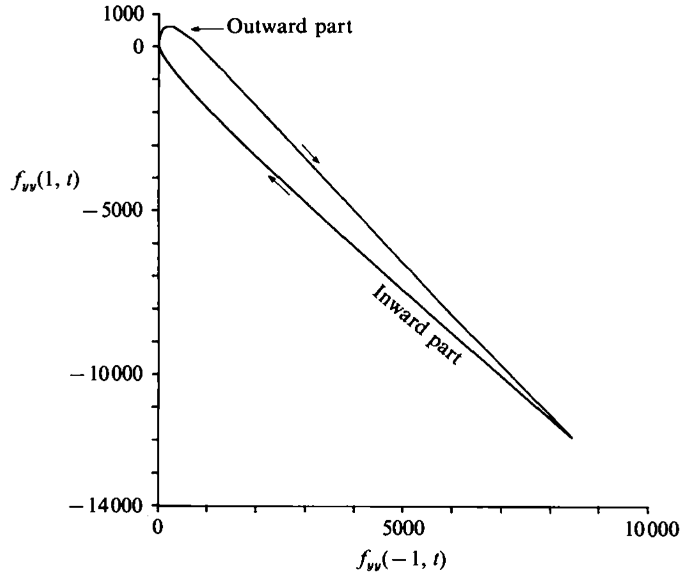

FIGURE 9. Stable limit cycle of (6), (7) when $\epsilon = 1$ and $R = 40$. The slow viscous 'inward' part, and the explosive 'outward' part are marked.

is true for a wide range of initial conditions, $f_0(y)$. For $1 \gg R - R_{\text{Hopf}} > 0$, we find the only stable solution to be the limit cycle born in the (supercritical) Hopf bifurcation. In the range $6.4 \leqslant R \leqslant 40$ where we have done calculations, a Fourier analysis indicates that the solution remains periodic, and does not become quasi-periodic or chaotic, nor does it undergo period doubling. The solution does, however, grow rapidly with increasing R and becomes difficult to compute reliably for values of R greater than about 40.

We analyse below two parts of the limit cycle, which we name according to their journey to and from small amplitudes: an 'inward' part, and an 'outward' part. (See figure 9, where we have projected $f(y,t)$ to the phase plane whose variables are $x_1 = f_{yy}(-1,t)$ and $x_2 = f_{yy}(1,t)$.) The 'inward' part has an inviscid sinusoidal solution away from the walls, whose amplitude is slowly diminished by viscous dissipation, while the 'outward' part has an inviscid solution away from the walls which grows rapidly in amplitude by inviscid means, and would become singular in a finite time were it not moderated by viscosity near one of the walls. This explosive growth in the 'outward' part is responsible for the numerical difficulties we encounter.

4.1. *Inward part of limit cycle*

On the inward part, $f(y,t)$ changes slowly in time and, away from the walls, is approximately sinusoidal, $f(y,t) \approx A(t)\cos \pi y$. Inserting this ansatz into (6), we find that the amplitude A decays exponentially, $A(t) \approx A(t_0)\exp\{-\pi^2(t-t_0)/R\}$. This is then the slow viscous decay of the inviscid sinusoidal velocity profile. (Our numerical results are in agreement with this, see figure 10 for the exponential decay.)

4.2. *Outward part of limit cycle*

On the outward part, f_y is at first approximately constant on the lowest three-quarters of the channel (away from the lower boundary layer) and is positive there, so there is flow away from $x = 0$. In the upper part of the channel (again away from the boundary layer) f_y has a minimum. As time advances, the magnitude of f_y

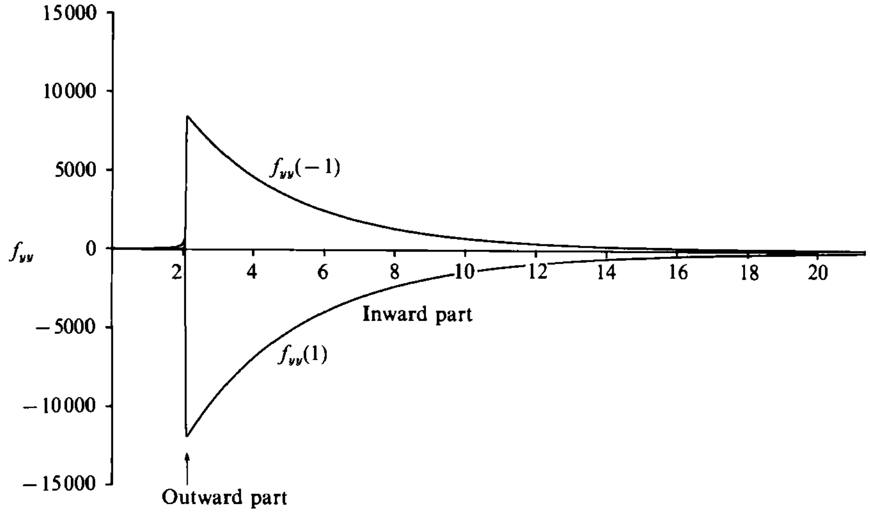

FIGURE 10. Time series of $f_{yy}(-1,t)$ and $f_{yy}(1,t)$ for the limit cycle in figure 9. The slow exponential viscous decay of the 'inward' part and the explosive growth of the 'outward' part are indicated. (The quantity $f_{yy}(\pm 1)$ is proportional to the skin friction at the walls.)

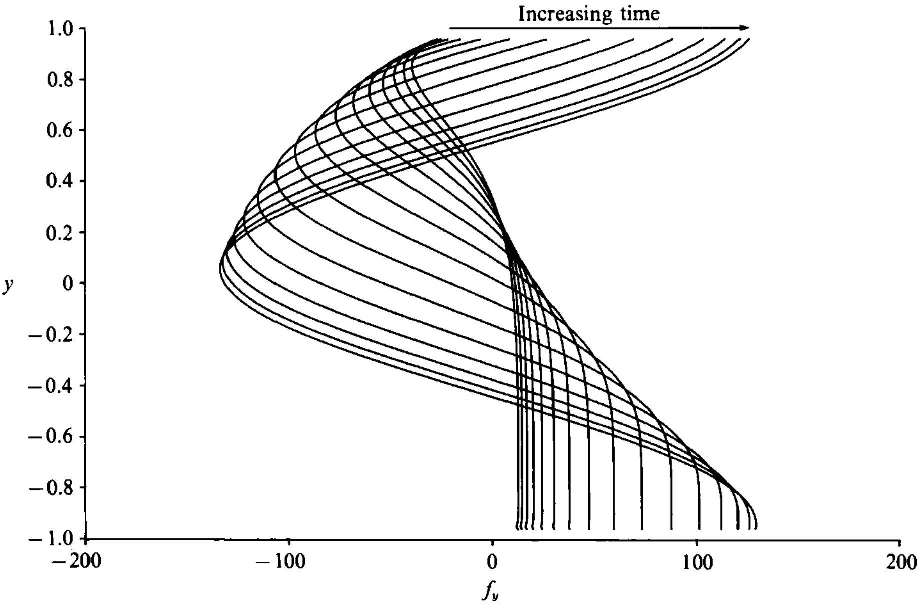

FIGURE 11. Velocity profiles f_y against y at successive time intervals of 0.02 s, during the outward part of the limit cycle in figure 9.

increases and its minimum occurs at successively smaller values of y, that is, the 'hump' moves towards the lower wall (see figure 11). Analysing $f_y(y,t)$ and $f_{yy}(y,t)$ before the hump gets too close to the lower wall, we find: (i) $\max f_y(y,t) \propto (t_s-t)^{-1}$ and $\min f_y(y,t) \propto (t_s-t)^{-1}$ as $t \rightarrow t_s$, for some 'singularity time', t_s; (ii) there is a local minimum of $f_{yy}(y,t)$ which occurs near the top of the channel, at $y_{\min}(t)$, say – if we plot $\min f_{yy}(y,t)$ against $y_{\min}(t)$ at successive times we find a straight line, $\min f_{yy} = a y_{\min}(t)+b$; and (iii) in the lower region of the channel $f_{yy} \approx 0$, and in the upper region the profile is very nearly sinusoidal.

Away from the walls the solution appears to have the similarity form

$$f(y,t) = (t_s - t)^{-p}\,\phi(\eta), \tag{26}$$

where

$$(\eta - \eta_0) = (y - y_0)\,(t_s - t)^{-q}. \tag{27}$$

Then comment (i) implies that $p+q = 1$, and (ii) implies that $p+2q = -q$, so $p = \frac{3}{2}$ and $q = -\frac{1}{2}$. (We distinguish between general solutions of the Berman problem, which are all of the similarity form where $\Psi = xf(y,t)$, and solutions f which have the further self-similarity of (26), (27). In this section 'similarity solution' will mean the latter, which, in the terminology of Barenblatt & Zel'dovich (1972), is an *intermediate asymptotic*.)

Since $q < 0$ no shock develops. Instead the hump spreads out as time advances. This phenomenon is inviscid: after substituting the ansatz (26), (27) into the Proudman–Johnson equation (6) the viscous term is a factor of the order $(t_s - t)^2\,\nu$ smaller than the other terms as $t \rightarrow t_s$ (away from the boundary layers).

Clearly the similarity solution (26) blows up as $t \rightarrow t_s$, but the full solution of (6) cannot blow up in the same way because the walls at $y = \pm 1$ prevent the indefinite spreading of the velocity profile. Instead, when the hump gets close to the lower wall some moderating viscous mechanism enables the solution to round the 'south-east corner' (the 'sharp end') of the limit cycle and begin the inward part. Before this viscous moderation, the solution f becomes large, and in particular there are large gradients in f in the boundary layers. For example, the most extreme values of the quantities $f_{yy}(\pm 1, t)$ on the limit cycle (which occur at the 'south-east corner') seem to grow like R^p as R is increased (where $p \approx 4$). Indeed, for R greater than about 40, the numerical solution 'blows up', that is, we encounter numerical overflow. Refining the spatial grid removes the overflow for a given R, but successive increases in R require ever finer grids. The power-law growth of the limit cycle with increasing R is some evidence that the limit cycle exists for all $R > R_{\mathrm{Hopf}}$, and therefore that the numerical overflow does not represent a true finite-time mathematical singularity in the exact solution f of the Proudman–Johnson equation. We return to this point later.

The similarity solution $\phi(\eta)$ satisfies the equation

$$\tfrac{1}{2}\phi'' - \tfrac{1}{2}\eta\phi''' = \phi\phi''' - \phi'\phi'' + \delta\phi^{\mathrm{iv}}, \tag{28}$$

where $\delta = \nu(t_s - t)^2$. We are interested in the limit as $\nu \rightarrow 0$ and as $t \rightarrow t_s$ so that δ is small. Ignoring then the viscous term in (28), we may combine a linear and a sinusoidal profile for ϕ to give the observed numerical profile during the outward part of the limit cycle, away from the boundary layers. That is,

$$\left.\begin{aligned} \phi &= -\tfrac{1}{2}\eta + k(\eta - \eta_0) && \text{for} \quad \eta < \eta_0 \\ \phi &= -\tfrac{1}{2}\eta + ak\sin\left((\eta - \eta_0)/a\right) && \text{for} \quad \eta > \eta_0 \end{aligned}\right\}, \tag{29}$$

for some constant a, where $k = b^{\frac{1}{2}}$, $b = (t_s - t)^2\,\beta + \frac{1}{4}$, and β is the pressure coefficient as in §2. From a numerical fit of f_y^{-1} against t in the region $\eta < \eta_0$, we find $\phi' \approx 0.757$, and so $k \approx 1.257$, when $R = 40$. At the matching point $(\eta = \eta_0)$, ϕ, ϕ' and ϕ'' are continuous, but ϕ''' is not – a viscous layer acts in a thin region around $\eta = \eta_0$ to smooth ϕ''' there, as for the steady solution described in §3.5.1 (Proudman 1960). The thickness of the viscous matching region is $|\eta - \eta_0| = O(\delta^{\frac{1}{2}}) = O(\nu^{\frac{1}{2}}(t_s - t))$. In terms of y this region has thickness of order $\nu^{\frac{1}{2}}(t_s - t)^{\frac{1}{2}}$. The viscous layer therefore becomes very thin both as $\nu \rightarrow 0$ and as $t \rightarrow t_s$ (so do the boundary layers near the walls $y = \pm 1$).

This is one reason why the numerical code runs into difficulties as R is increased: the spatial grid is too coarse to resolve the viscous layers.

5. Finite-time singularities in the Euler and Navier–Stokes equations

We have described above how the solutions of the Proudman–Johnson equation grow rapidly in amplitude as the Reynolds number (based on the suction velocity through the wall) increases, and how we encounter numerical overflow when we try to calculate large-R flows. We have not interpreted the numerical overflow as a mathematical singularity because the overflow can always (in our experience) be removed by refining the spatial grid sufficiently. There is, however, great interest at present in the finite-time blow-up of solutions of the Euler and Navier–Stokes equations (see, for example, Childress *et al.* 1989; Stuart 1988), so it seems appropriate to examine the explosive 'outward' part of the limit cycle further. Since it is a viscous effect that prevents f from becoming singular as $t \rightarrow t_s$, we consider now what would happen in the absence of viscosity.

Stuart (1988) has given examples of three-dimensional solutions of the Euler equations in an unbounded domain which blow up in a finite time. There is a single characteristic on which the solution becomes singular as $t \rightarrow t_s$, the singularity time. Similarly, Calogero (1984) has shown that, for example, the equation

$$w_{xt} + w_{xx} w + \lambda + \mu w_x + \nu w_x^2 = 0 \tag{30}$$

can be solved by quadratures, where λ, μ, ν are constants, and that given suitable (but very general) initial conditions a solution $w(x,t)$ can blow up in a finite time, along one characteristic. This equation is a generalized version of the Proudman–Johnson PDE, where $w(x,t) = -f(y,t)$ and the viscous term is ignored.

It is easy to construct solutions of the Euler equations in an unbounded domain which blow up in a finite time: there are similarity solutions which have the singularity as $t \rightarrow t_s$ built in (for example, if the solution is of the form $U/(t_s - t)$). The interesting feature of Stuart's solutions of the Euler equations (and Calogero's solutions of similar equations) is that their singular behaviour is not built-in, but arises naturally for a wide class of initial conditions. In our case, in the Berman problem, we have shown that an essentially inviscid phase arises naturally as an *intermediate asymptotic* (Barenblatt & Zel'dovich 1972) of the full (viscous) problem, and that to a first approximation solutions in this inviscid phase become singular in a finite time, although for solutions of the full PDE a viscous moderating mechanism acts to prevent such a singularity. Our similarity solution, $(t_s - t)^{-\frac{3}{2}} \phi(\eta)$, as an exact solution of the Euler equations which exhibits blow-up, is of no great interest. Rather what is of interest is that this inviscid solution should arise spontaneously from a non-singular limit-cycle solution of the full viscous PDE. We have already described its similarity form in (26), (27). Now we offer an alternative description in terms of characteristics.

If the viscous term νf_{yyyy} is omitted then the Proudman–Johnson equation (6) may be cast in the form of a quasi-linear PDE for $u(y,t)$ (up to a multiplicative factor of x),

$$u_t - f(y,t)\, u_y = \beta - u^2, \tag{31}$$

which we can solve by the method of characteristics (Stuart 1988 and Calogero 1984, modified to allow for the singularity in the pressure coefficient, β, as $t \rightarrow t_s$). Thus we solve $\partial Y(\zeta,t)/\partial t = -f$ for $y = Y(\zeta,t)$, the characteristics; and $\partial U(\zeta,t)/\partial t = \beta - U^2$ for the velocity, $u(y,t) = U(\zeta,t)$. The characteristic variable is ζ.

We find the velocity to be

$$U(\zeta, t) = \frac{1}{t_s - t}\left[\frac{k\{1+\alpha(\zeta)\,(t_s-t)^{2k}\}}{1-\alpha(\zeta)\,(t_s-t)^{2k}} - \frac{1}{2}\right], \tag{32}$$

where $\alpha(\zeta) = t_s^{-2k}(t_s\,U(\zeta,0) - k + \frac{1}{2})/(t_s\,U(\zeta,0) + k + \frac{1}{2})$. The characteristics are given by

$$Y(\zeta, t) = y_0 + \int_0^{\zeta} \exp\left\{-\int^{t} U(\zeta', t')\,\mathrm{d}t'\right\}\mathrm{d}\zeta'. \tag{33}$$

Insight into the behaviour of the characteristics is gained by expanding these expressions for U and Y near $t = t_s$. From (32), we find that

$$U(\zeta, t) \sim (k - \tfrac{1}{2})\,(t_s - t)^{-1} + \ldots \quad \text{as} \quad t \to t_s.$$

This intermediate asymptotic, where the velocity is proportional to $(t_s - t)^{-1}$, is indeed that observed in our numerical integrations (see §4.2). From (33), we find that on any given characteristic

$$(y - y_0) \propto (\zeta - \zeta_0)\,(t_s - t)^{k-\frac{1}{2}} \quad \text{as} \quad t \to t_s. \tag{34}$$

Recall that when $R = 40$, for example, $k \approx 1.257$, so that the characteristics become increasingly bunched together as $t \to t_s$, although the velocity profile spreads out in that limit. We conclude that although the description of f in terms of characteristics is the more physically meaningful, the description in terms of the similarity variable η is the more revealing.

Childress *et al.* (1989) have recently considered two-dimensional viscous flow of the Berman similarity form (that is, in our notation $(u, v) = (xf_y(y, t), -f(y, t))$) in a channel with parallel, *impermeable* walls; the boundary conditions on f and f_y at the walls are then homogeneous. A Reynolds number *of the flow* is defined to be

$$R(t) = \nu^{-1}\left\{\int_{-L/2}^{L/2} f_y^2(y, t)\,\mathrm{d}y\,L^3\right\}^{\frac{1}{2}}, \tag{35}$$

where ν is the kinematic viscosity of the fluid, and L the width of the channel. (Recall that the Reynolds number for the Berman problem involves the wall-suction velocities, and is independent of the flow which is driven in the channel.) They show analytically that when the initial Reynolds number, $R_0 \equiv R(0)$, is below about 16.212 then the velocity profile decays to zero as $t \to \infty$. Numerical integrations are carried out for these stagnation-point flows for a range of $R_0 > 16.212$, and in a typical integration, with $R_0 = 6400$, machine overflow occurs in a finite time ($t_s \approx 1.50$). This 'blow-up' is interpreted as evidence of a mathematical singularity in the solution of the Proudman–Johnson PDE. Indeed, Childress *et al.* find that just before the blow-up,

$$R^{-1}(t) \propto (t_s - t), \tag{36}$$

where t_s is the singularity time. Their velocity profiles, however, become ragged as the singularity time is approached. We found that similarly ragged velocity profiles arose in our numerical solutions of the Berman problem when too coarse a spatial grid was chosen – refining the grid always removed the raggedness. Indeed, in a personal communication, Childress reports that in subsequent numerical integrations their numerical overflow can also always be removed by choosing a suitably fine spatial grid. This implies that the numerical overflow which they observe does not represent a mathematical singularity in exact solutions f. It may be that for sufficiently large R_0 (or R) a true mathematical singularity develops in solutions of the Proudman–Johnson equation with homogeneous (or suction) boundary conditions. This is an open question. Alternatively, it may be possible to construct an inertial manifold for the Proudman–Johnson equation, and prove that solutions must remain bounded for all times, and that there can be no finite-time singularities, as has been done for other dissipative PDEs, such as the Kuramoto–Sivashinsky equation (Foias *et al.* 1988), and the complex Ginzburg–Landau equation (Doering *et al.* 1988).

6. The transition to chaos

6.1. *The transition to chaos in the symmetric problem*

Zaturska *et al.* (1988) have calculated time-dependent solutions of the symmetric Berman problem by numerically integrating the Proudman–Johnson equation (6) subject to boundary conditions (7), with $\epsilon = 0$. They describe the bifurcations of the solutions as R is increased. There is an abrupt transition from simple to complicated dynamics as R increases through a threshold value, R_{hom}. This transition is a so-called 'homoclinic-explosion' (Sparrow 1982), and is directly analogous to that in Lorenz' system of three ODEs (Lorenz 1963). It is this analogy which we exploit in this section when we interpret the numerical results that we present for slightly asymmetric problems (where $0 < |\epsilon| \ll 1$). The abruptness of the appearance of chaos in time-dependent solutions of the symmetric problem is a consequence of the symmetry, just as the pitchfork bifurcation of the steady solutions is when $R = R_1 \approx 6.001353$. The theory of 'Lorenz-like' dynamical systems (Glendinning 1987) predicts a smooth route to chaos for slightly asymmetric Berman problems. Our aim in this section is to apply Glendinning's theory and *unfold* the 'homoclinic explosion' of the symmetric problem. That is, we describe the wider range of behaviour which is possible when both R and ϵ may be independently varied. (When there is symmetry ($\epsilon = 0$), we may vary only R, and thereby take a one-dimensional cross-section through the two-dimensional (R, ϵ)-parameter space.)

The theory we shall apply holds strictly for three-dimensional dynamical systems (Glendinning 1987), although we shall apply it to our infinite-dimensional system, the Proudman–Johnson equation (6). We believe ourselves to be justified in this (although we cannot prove it) because our numerical results suggest that for general values of R and ϵ, solutions $f(y,t)$ are rapidly confined to some low-dimensional submanifold of the infinite-dimensional function space in which they lie. Therefore the system is effectively low-dimensional; its dynamics are essentially determined by a small number of *modes*. This is a common feature of dissipative PDEs, for example, the Kuramoto–Sivashinsky equation (Foias *et al.* 1988). The rapid attraction of solutions to a limit cycle (which has dimension one) when R is large and $\epsilon = 1$ exemplifies the effective low-dimensionality of the Proudman–Johnson equation.

We shall take the geometric view that $f(y,t)$ evolves along some trajectory in its function space, and assume that we can understand its behaviour by thinking of it as evolving in $\mathbb{R}^3$, after some initial transients. We thus assume the existence of an *inertial manifold* for the Proudman–Johnson equation, of dimension not greater than three for the values of R and ϵ of interest (we cannot prove the existence of such an inertial manifold). This assumption is crucial to our interpretation of the transition to chaos.

In order to present solutions $f(y,t)$, we project them into $\mathbb{R}^2$. Under projection, steady solutions $F(y)$ become fixed points and periodic solutions become closed periodic orbits, for example. As before, we shall take $x_1 = f_{yy}(-1,t)$ and $x_2 = f_{yy}(1,

t) as our phase-plane variables. When $\epsilon = 0$, the invariance of (6), (7) under the mapping $f(y,t) \mapsto -f(-y,t)$ (a symmetry which corresponds to flipping the channel about its centreline) implies that to every trajectory in the phase plane there corresponds another which is its image under reflection in the line $\mathscr{L} = \{(x_1, x_2): x_1 + x_2 = 0\}$.

A summary of the numerical results of Zaturska *et al.* (1988) will provide a background for our own results. The language of this section will be largely that of dynamical systems (see, for example, Guckenheimer & Holmes 1986) – we have tried to keep the jargon to a minimum, and to explain those specialized terms we use. Nevertheless, this section may seem rather confusing for the reader who is not used to the dynamical systems approach. For such a reader, the essential result may be summarized as follows. The chaotic (aperiodic) solutions found by Zaturska *et al.* for the symmetric problem are predicted by the theory of dynamical systems to persist when $\epsilon \neq 0$. This qualitative statement is true, but in practice it turns out that the symmetry need be perturbed only very slightly for the chaotic solutions to be replaced by more regular, periodic solutions.

For the rest of this section we consider $R > R_{11} \approx 12.963$, where the interesting bifurcations occur.

The fixed point I (which represents the steady solution of type I) is a saddle, with a one-dimensional unstable manifold, $W^{\mathrm{u}}(I)$, and leading (that is, least negative) eigenvalues of the linear stability problem (14): $\lambda_1, \lambda_2, \lambda_3 \in \mathbb{R}$ satisfying

$$\lambda_1 > 0 > \lambda_2 > \lambda_3 \quad \text{and} \quad -\lambda_2/\lambda_1 < 1. \tag{37}$$

(The *unstable manifold* of a fixed point I of a dynamical system is the set of points which approach I when run backwards in time, in the limit as $t \to -\infty$.) These are technical conditions required of the eigenvalues by Glendinning's theory, which will be applied later. Similarly each of the steady solutions of types I_1 and I_1' has a two-dimensional unstable manifold. (Recall that I_1 and I_1' are the pair of asymmetric steady solutions born in the pitchfork bifurcation when $R = R_1$. In the phase plane they are mirror images in the line $\mathscr{L}$, that is, I_1' is obtained from I_1 by flipping the channel about its centreline.) These solutions of types I_1 and I_1' have become unstable through supercritical Hopf bifurcations, and there are stable periodic orbits, $\mathscr{C}_1$ and $\mathscr{C}_1'$, around them (figure 12*b*). These periodic orbits grow, then undergo a sequence of bifurcations as R is increased (in particular they become quasi-periodic tori, and may become aperiodic). However, they 'remain quantitatively close to simple loops in phase-space' (Zaturska *et al.*). It appears from numerical integrations that these two orbits are the only attractors of the system for $R < R_{\mathrm{hom}}$ ($R_{\mathrm{hom}} < 20$). In particular, general trajectories eventually remain on one side or other of the symmetry line, $\mathscr{L}$. To conform with later notation we shall assign to each orbit a code – a 0 (or 1) if the orbit lies below (or above) $\mathscr{L}$ (figure 12). (With reference to the figure, 'above $\mathscr{L}$' means $x_1 + x_2 > 0$, and 'below' the converse.) For example, the orbit $\mathscr{C}_1$ close to I_1 has code 1, and the orbit $\mathscr{C}_1'$ close to I_1' has code 0.

As R is increased, $\mathscr{C}_1$ and $\mathscr{C}_1'$ grow, then a pair of orbits which are homoclinic to the fixed point I is formed, when $R = R_{\mathrm{hom}}$ (see figure 12*c*). For $R > R_{\mathrm{hom}}$ aperiodic solutions are found which cross $\mathscr{L}$ in a seemingly random fashion. (Of course the solutions are deterministic, but their behaviour appears random because there is exponential separation of nearby trajectories, and sensitivity to initial position.) This abrupt transition to chaos as R increases through R_{hom} is the 'homoclinic explosion' (so called because an infinite number of bifurcations occurs simultaneously, see Glendinning 1987).

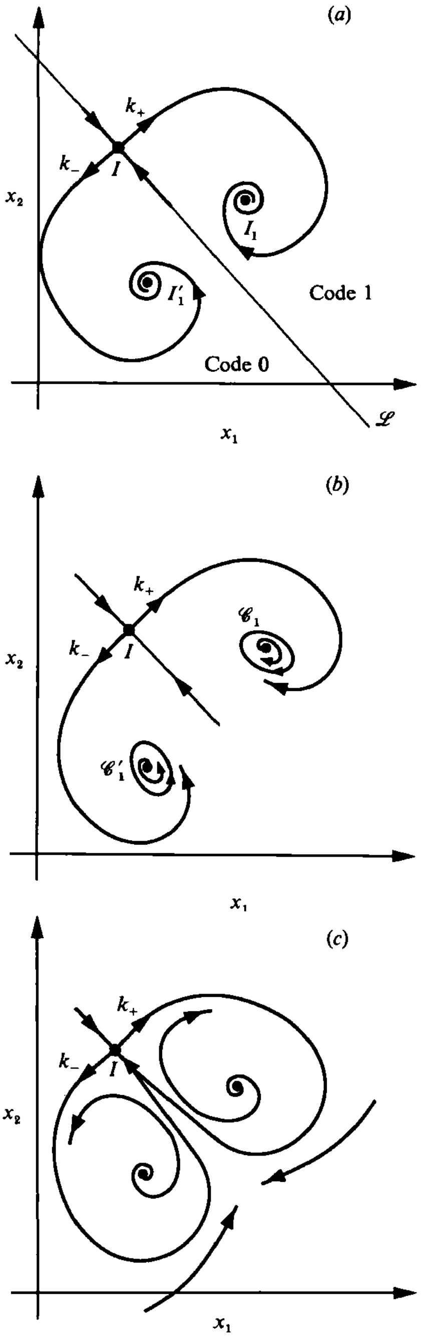

FIGURE 12. Schematic of the (x_1, x_2)-phase plane for $\epsilon = 0$. The symmetry of the Berman problem under reflection about the centreline of the channel induces a symmetry in the phase plane about the line $\mathscr{L}$. The fixed point I represents the steady solution of type I, and $k_\pm$ denote the two branches of its unstable manifold, $W^u(I)$. The fixed points I_1 and I'_1 represent the solutions of types I_1 and I'_1, which are images of one another under reflection in $\mathscr{L}$. (a) $R_1 < R < R_{11}$. Any initial condition not on the stable manifold of I evolves under (6) to either I_1 or I'_1 as $t \to \infty$. (b) $R_{11} < R < R_{\text{hom}}$. Most trajectories asymptote to one of the orbits $\mathscr{C}_1$ or $\mathscr{C}'_1$ as $t \to \infty$. (c) $R = R_{\text{hom}}$. A pair of homoclinic orbits to I, in the butterfly configuration. (We need to consider I in at least three-dimensional space for this configuration to be possible.)

Before we proceed to describe Glendinning's theory, we need to extend somewhat the results of Zaturska *et al.* for the symmetric system, and set up some more notation. The unstable manifold of I has two branches: k_- which leaves I below $\mathscr{L}$, and k_+ which leaves I above $\mathscr{L}$ (see figure 12). To each of these branches we can assign its *kneading sequence*, a semi-infinite sequence of 0s and 1s which describes the loops that it makes in phase space above and below $\mathscr{L}$. (The kneading sequence is defined similarly for arbitrary trajectories, and essentially captures all of their interesting dynamics.) We can determine the kneading sequence for $k_\pm$ numerically by choosing an appropriate initial condition, $f_0(y)$. (This will be the steady solution I plus a small multiple of the unstable eigenmode, g_1, i.e. we start a little distance along $W^u(I)$ from I.) We find that for $R \leqslant 19.6$, $k_- = 000\ldots$ (and by symmetry $k_+ = 111\ldots$), while for $R = 19.7$, $k_- = 0111\ldots$ (and $k_+ = 1000\ldots$), see figure 13. (The reference to both the unstable manifold and its kneading sequence as $k_\pm$ is strictly an abuse of notation.) From this we conclude that for some intermediate value of R, R_{hom}, both branches of the unstable manifold of I return to I as $t \rightarrow \infty$, that is, a pair of homoclinic orbits is formed. Figure 13 shows the homoclinic orbit formed by k_- when $R = R_{\text{hom}}$. That of k_+ is its mirror image in the symmetry line $\mathscr{L}$. (A trajectory $\boldsymbol{x}(t) = (x_1, x_2)$ is a *homoclinic orbit* to I if $\boldsymbol{x}(t) \rightarrow I$ as $t \rightarrow -\infty$ and as $t \rightarrow \infty$.) This pair of homoclinic orbits lies in the 'butterfly' configuration, where both orbits approach I in the same direction as $t \rightarrow \infty$. It is the formation of this pair of homoclinic orbits in the butterfly configuration which makes the Proudman–Johnson equation with equal-suction boundary conditions 'Lorenz-like' (Glendinning 1987; Sparrow 1982; Lorenz 1963).

6.2. *Breaking the symmetry*: *the codimension-two unfolding*

So far, our presentation of results has been motivated by Glendinning's theory which describes a codimension-two (that is, two-parameter) *unfolding* of the homoclinic explosion. In particular, this theory describes how the transition to chaos is more gentle when the symmetry of the 'Lorenz-like' dynamical system is broken (in our case, when $\epsilon \neq 0$).

Glendinning considers a family of three first-order ordinary differential equations which has two parameters, denoted by μ_0 and μ_1. These parameters have a definition which is convenient for discussing the bifurcation structure of the dynamical system, but which is otherwise rather complicated (Glendinning 1987). The family of ODEs is 'Lorenz-like' if the following assumptions are made. First, there is a saddle point, O, which has a one-dimensional unstable manifold, $W^u(O)$, for all parameter values. Secondly, the parameters are defined so that when $\mu_0 = 0$ there is a homoclinic orbit (denoted by Γ_0) to the fixed point O formed by one branch of the unstable manifold; and when $\mu_1 = 0$ the other branch similarly forms a homoclinic orbit, Γ_1. Thirdly, when both μ_0 and μ_1 are zero, there are two homoclinic orbits to O which are in the butterfly configuration. Finally, the fixed point O has real eigenvalues $\lambda_{1,2,3}$ which satisfy

$$\lambda_1 > 0 > \lambda_2 > \lambda_3 \quad \text{and} \quad -\lambda_2/\lambda_1 < 1. \tag{38}$$

Under these assumptions, Glendinning describes the bifurcations of the system for small values of the parameters, in a neighbourhood of the homoclinic orbits $\Gamma_{0,1}$ in phase space: there are eight regions in (μ_0, μ_1)-space in which the kneading sequences of the two branches of $W^u(O)$ are given. In particular a region in the first quadrant of parameter space is shown to give systems with complicated dynamics (region 8 in figure 14).

Clearly, in applying Glendinning's theory to the Berman problem we shall identify

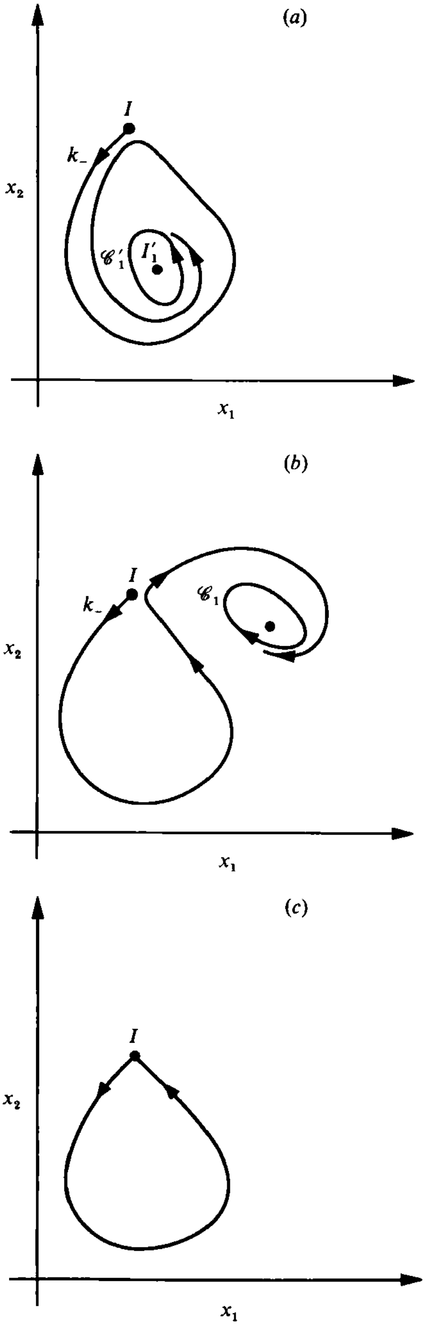

FIGURE 13. Schematic, and selective picture of the (x_1, x_2)-phase plane. (Only those features relevant to the behaviour of k_- are shown.) The evidence for a homoclinic orbit from k_-: For (a) $R \leqslant 19.6$, k_- has kneading sequence 000 ..., and asymptotes to $\mathscr{C}_1'$ as $t \rightarrow \infty$; (b) For $R \geqslant 19.7$, k_- has kneading sequence 0111 ... and asymptotes to $\mathscr{C}_1$ as $t \rightarrow \infty$. Therefore, (c), we conclude that for some intermediate value of R there is a homoclinic orbit to I from k_-. By symmetry there is also a homoclinic orbit from k_+ at this value of R.

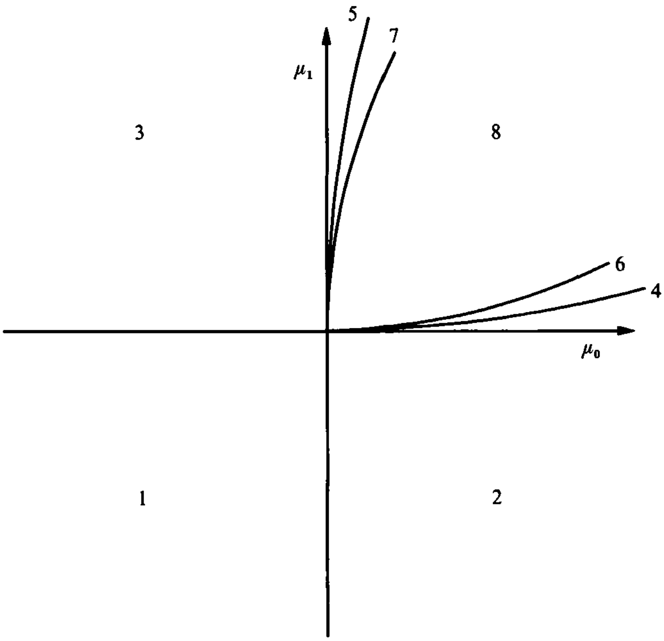

FIGURE 14. The eight regions in (μ_0, μ_1)-parameter space. There are complicated dynamics in region 8 in the first quadrant (see Glendinning 1987).

his fixed point, O, with ours, I, and our main task will be to relate his parameters (μ_0, μ_1), to ours, (R, ϵ) close to $(R_{\text{hom}}, 0)$. Our assumption that close to homoclinicity the dynamics of the Proudman–Johnson PDE are essentially three-dimensional is crucial to this application.

The symmetries of our system and of Glendinning's model imply that the line $\epsilon = 0$ must correspond to the line $\mu_0 = \mu_1$. (For suppose we reflect phase-plane trajectories in the line $\mathscr{L}$. On the one hand this is equivalent to the map $\epsilon \mapsto -\epsilon, f(y, t) \mapsto -f(-y, t)$, which reflects the parameter ϵ in the line $\epsilon = 0$. Alternatively, this interchanges the role of μ_0 and μ_1, which corresponds to reflection in the line $\mu_0 = \mu_1$. Therefore the lines $\epsilon = 0$ and $\mu_0 = \mu_1$ are identical.) Thus for $\epsilon = 0$, increasing R corresponds to moving along the line $\mu_0 = \mu_1$ from the third to the first quadrant in (μ_0, μ_1)-space (see figure 15, which shows the qualitative relationship between (R, ϵ) and (μ_0, μ_1) for sufficiently small $|(\mu_0, \mu_1)|$).

To illustrate the consequences of Glendinning's theory for the Berman problem near symmetry, consider the bifurcations which are predicted as R is increased for some fixed, small, non-zero ϵ. That is, consider the bifurcations along a line $\epsilon = \epsilon_0$ in (R, ϵ)-space. On increasing R (see figure 15) we should cut first the line $\mu_0 = 0$ then the line $\mu_1 = 0$, and so there should first be a homoclinic orbit from one branch (k_-) of $W^{\text{u}}(I)$ then a homoclinic orbit from the other (k_+), by definition of μ_0 and μ_1. These two homoclinic orbits will be formed at different values of R because we have broken the symmetry of the problem. By numerical integration of the Proudman–Johnson equation to find $k_\pm$ for a variety of small positive ϵ, we aim to locate those parameter values (R, ϵ) which lie on either the μ_0-axis or the μ_1-axis, and thereby determine the relationship between the two sets of parameters. Then we can apply Glendinning's theory to predict the bifurcations of the Berman problem in terms of R and ϵ, and find where the system has complicated dynamics.

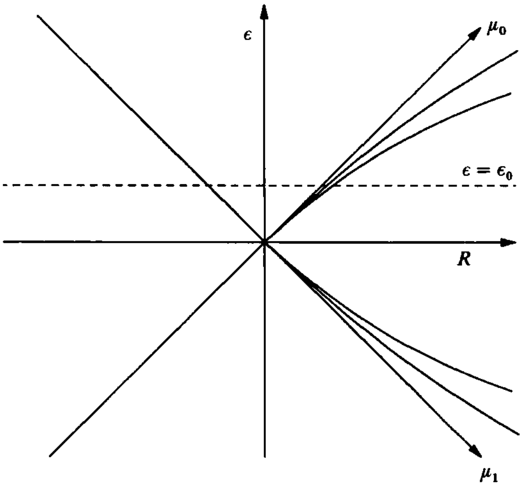

FIGURE 15. The qualitative relationship between parameters (R, ϵ) and (μ_0, μ_1). A typical line $\epsilon = \epsilon_0$ is shown (the dashed line) – note that it passes through regions 1, 2, 4, 6, 8 as R is increased. Thus there should a smooth transition from simple dynamics (in region 1) to complicated dynamics (in region 8) for slightly asymmetric Berman problems. The origin is $(R, \epsilon) = (R_{\text{hom}}, 0)$, $(\mu_0, \mu_1) = (0, 0)$.

(We should clarify the term 'complicated dynamics' with which we have described solutions of the symmetric Berman problem for $R > R_{\text{hom}}$. We have assumed that the aperiodic solutions found by Zaturska *et al.* lie on a strange attractor, although they could conceivably be just long-term chaotic transients, hence our rather vague description of them. The complicated dynamics predicted by Glendinning's theory arise from the birth of a strange invariant set, when the homoclinic connection forms. This invariant set, however, is not attracting for any of the parameter values in Glendinning's (local) analysis, although it has a profound effect on solutions by introducing chaotic transients. A strange attractor may be formed at larger values of μ_0 and μ_1 than those considered by Glendinning (Afraimovich & Shil'nikov 1983).)

Much of the discussion above may seem rather abstract and remote from fluid mechanics. We therefore provide an illustrative example, and describe some typical numerical results from integrations of (6) for small ϵ.

6.3. *Numerical results for* $\epsilon = 1/39 \approx 0.02564$

A good illustrative example of our numerical integrations of (6), (7) for small ϵ is when $\epsilon = \frac{1}{39}$ – we should observe the scenario described above as we increase R.

For $R \leqslant 13.372$, $k_+ = 111\ldots$ and $k_- = 000\ldots$. Each branch of $W^u(I)$ lies in the stable manifold of a periodic orbit: k_- asymptotes to $\mathscr{C}_1'$ as $t \to \infty$, and k_+ asymptotes to $\mathscr{C}_1$ as $t \to \infty$. $\mathscr{C}_1$ and $\mathscr{C}_1'$ are stable periodic orbits created from supercritical Hopf bifurcations of the steady solutions I_1 and I_1' respectively. (They appear to remain periodic, and do not become, for example, quasi-periodic or chaotic, as the corresponding solutions do when $\epsilon = 0$.) These stable orbits are irrelevant to Glendinning's theory, since they are outside the neighbourhood of the homoclinic orbits where the theory applies. We conclude that for $R \leqslant 13.372$ we are in region 1 of (μ_0, μ_1)-space (see Glendinning 1987).

When $R = 13.382$, $k_+ = 111\ldots$ and $k_- = 0111\ldots$, and we are now in region 2 of (μ_0, μ_1)-space (Glendinning 1987). We conclude that for some $R = R_{\text{hom}-}$, where $R_{\text{hom}-} \in (13.372, 13.382)$, a homoclinic orbit Γ_0 is formed by k_-. Note that a small change in

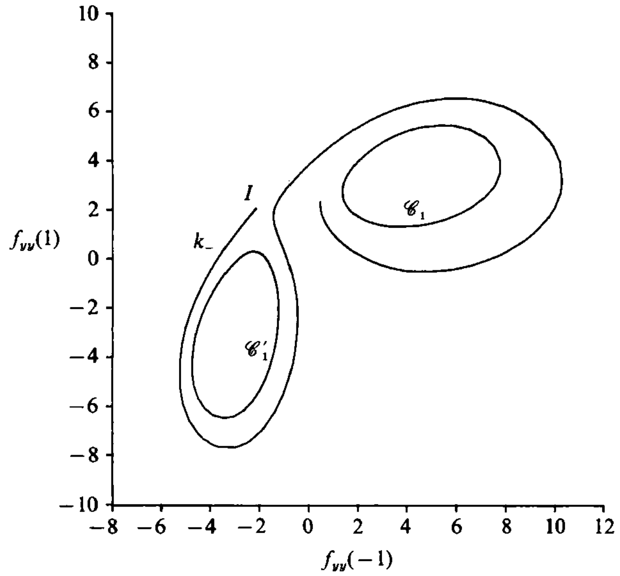

FIGURE 16. Three trajectories in $(f_{yy}(-1,t), f_{yy}(1,t))$-phase space when $\epsilon = \frac{1}{39}$ and $R = 13.528$. The two periodic orbits $\mathscr{C}_1$ and $\mathscr{C}'_1$ are shown, as is the lower branch of the unstable manifold of I, k_-, which has kneading sequence 0111....

ϵ (from 0 to $\frac{1}{39}$) has induced a large change in $R_{\text{hom}-}$ (from 19.6 to 13.4). This shows that a very small asymmetry in the problem may change the quantitative results by a large amount. We return to this point below.

Both orbits $\mathscr{C}_1$ and $\mathscr{C}'_1$ persist as R is increased through $R_{\text{hom}-}$, but for $R > R_{\text{hom}-}$ there is a further periodic orbit, Γ^u, 'a single non-stable periodic orbit with code 0' (Glendinning 1987) close to Γ_0.

As R is increased above 13.382, k_+ and k_- retain their codes and the stable orbits $\mathscr{C}_1$ and $\mathscr{C}'_1$ persist (figure 16). The periodic orbit $\mathscr{C}'_1$ is annihilated in a saddle-node bifurcation with the unstable orbit Γ^u for $R = R_{\text{sn}} \in (13.577, 13.601)$. The periodic orbits which have code 0 can be summarized in a diagram (see figure 17*a*) which shows the periods of the orbits plotted against R (cf. Glendinning & Sparrow 1984). A similar diagram for the symmetric case studied by Zaturska *et al.* is more complicated (see figure 17*b*): first, it has to indicate the quasi-periodic (and chaotic) orbits which arise from the periodic Hopf orbits; secondly, the details of which solution is shed from the homoclinic orbit Γ_0 are unknown. That is, we do not know whether each homoclinic orbit sheds an unstable solution which then coalesces with the appropriate stable Hopf orbit for some $R > R_{\text{hom}}$, as is the case when $\epsilon = \frac{1}{39}$ (see the right-hand diagram on figure 17*b*); or whether instead the stable $\mathscr{C}'_1$ simply grows until it collides with I as $R \rightarrow R_{\text{hom}}$ (see the left-hand diagram on figure 17*b*).

As R is increased above R_{sn}, $\mathscr{C}_1$ grows in size but does not meet I, and solutions from general initial conditions result in trajectories whose kneading sequences are eventually a string of 1s. In particular, $k_- = 0111\ldots$ and $k_+ = 111\ldots$ for all $R > R_{\text{hom}-}$. So we remain in region 2 and increasing R further does not take us across the line $\mu_1 = 0$. This seems to conflict with the schematic diagram in figure 15 which shows how the two sets of parameters (R, ϵ) and (μ_0, μ_1) are related, and where any line $\epsilon = \epsilon_0$ must cross both μ coordinate axes. The point is, however, that figure 15 is valid only in a neighbourhood of $(\mu_0, \mu_1) = (0, 0)$, and it is only in such a region that we expect an approximately linear relation between the two sets of parameters. This

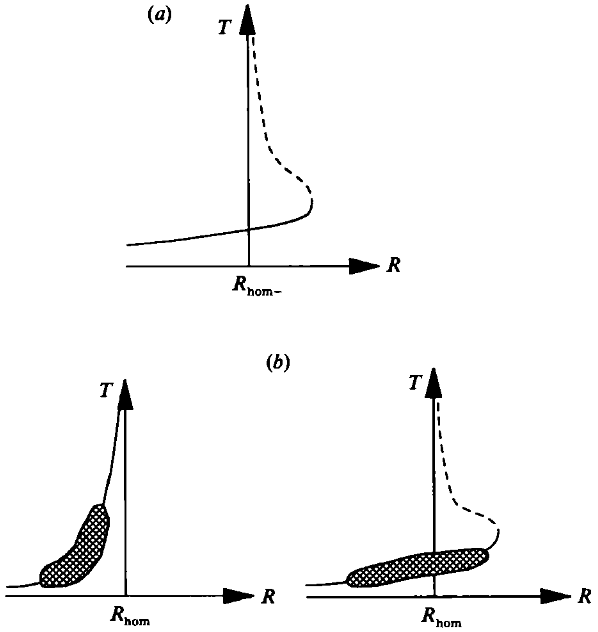

FIGURE 17. The period of those time-dependent solutions with code 0, plotted against R. (*a*) $\epsilon = \frac{1}{39}$. The solutions marked are the stable periodic orbit $\mathscr{C}_1'$ and the unstable periodic orbit which is shed from the lower homoclinic orbit Γ_0 (solid and dashed lines respectively). The stable periodic orbit persists through $R = R_{\text{hom}-} \approx 13.38$ and is destroyed in a saddle-node bifurcation at $R = R_{\text{sn}} \approx 13.6$. (*b*) Two possible scenarios for $\epsilon = 0$. The shaded region indicates quasi-periodic solutions with code 0. More, and more accurate, integrations would determine which scenario is the true one.

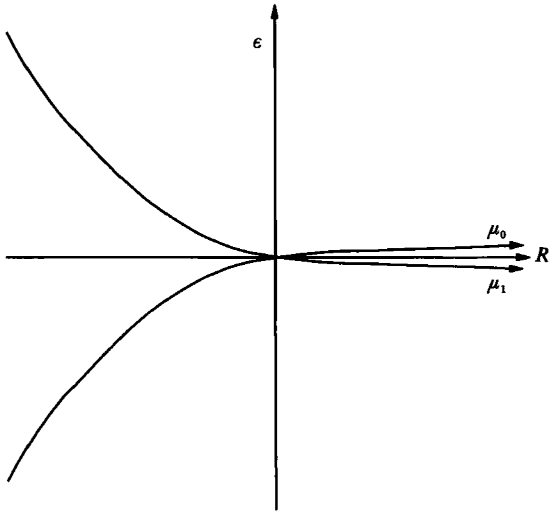

FIGURE 18. The relationship between (R, ϵ) and (μ_0, μ_1) is highly stretched. The positive quadrant in (μ_0, μ_1)-space occupies a very small region in (R, ϵ)-space, so a very slight asymmetry replaces complicated dynamics by simple dynamics. (Recall from figure 14 that the interesting dynamics occur in region 8, which lies in the positive quadrant in (μ_0, μ_1)-space.)

ϵ	$R_{\mathrm{hom}-}$
0	19.65 ± 0.05
0.000 25	16.7125 ± 0.0125
0.000 50	16.30 ± 0.05

TABLE 1. Values of the Reynolds number, $R_{\mathrm{hom}-}$, at which the lower branch, k_-, of the unstable manifold of I is homoclinic to I. Note the great change in $R_{\mathrm{hom}-}$ even with slight symmetry breaking.

means that for small enough ϵ_0 the line $\epsilon = \epsilon_0$ will cut both μ-axes (figure 15). Since the line $\epsilon = \frac{1}{39}$ cuts only the line $\mu_0 = 0$ we conclude that we need $|\epsilon_0| < \frac{1}{39}$ for figure 15 to represent accurately the relation between the two sets of parameters.

Figure 18 illustrates qualitatively (but more accurately than figure 15) how our numerical integrations for $\epsilon = \frac{1}{39}$ suggest that (R, ϵ) and (μ_0, μ_1) are related. The linear relationship of figure 15 is clearly very 'stretched', and so is valid only for extremely small $|\epsilon|$. The positive quadrant in (μ_0, μ_1)-space therefore occupies a very small region in (R, ϵ)-space, so that the Berman problem must be very close to symmetry to have complicated dynamics.

6.4. *Discussion*

Since the line $\epsilon = \frac{1}{39}$ does not cut the line $\mu_1 = 0$, it is clear that a small asymmetry in the time-dependent Berman problem has a surprising, disproportionate effect on the dynamics. In fact we have found no chaotic solutions of the Proudman–Johnson equation when $\epsilon = \frac{1}{39}$. An example of the large quantitative effect of slight symmetry breaking is shown in table 1, where values of $R_{\mathrm{hom}-}$ are given for various values of the symmetry-breaking parameter ϵ. (Recall that $R_{\mathrm{hom}-}$ is the value of R for which k_- first makes a homoclinic orbit to I, and that the curve $R = R_{\mathrm{hom}-}(\epsilon)$ is the curve $\mu_0 = 0$, by the definition of Glendinning 1987.) We estimate that $\mathrm{d}R_{\mathrm{hom}-}/\mathrm{d}\epsilon \approx (16.7125 - 19.65)/0.000\,25 \approx -10000$, when $\epsilon = 0$ (that is, the slopes of the μ_0 and μ_1 axes in (R, ϵ)-space are ± 0.0001). This shows the 'stretched' nature of the relationship between the two sets of parameters, as indicated schematically in figure 18. Region 8, which lies in the first quadrant in (μ_0, μ_1)-space, is clearly a very small region in (R, ϵ)-space.

Elsewhere (Cox 1989, 1990) we have shown that the Lorenz system itself may exhibit both the 'stretched' behaviour we have seen in the Berman problem and a 'nicer' relationship between the two sets of parameters, in two different cases. Although we do not understand the reasons why the Berman problem has such a small region of chaos, it is at least comforting to know that there are other systems where this behaviour occurs, even if it is not understood there either!

7. Conclusion

We have analysed similarity solutions of the Navier–Stokes equations for flow in a porous-walled channel. Such an analysis increases our repertoire of known 'exact' solutions, although, as with other similarity solutions, ours are physically unrealistic; the assumed form requires an infinite two-dimensional channel, and ignores three-dimensional disturbances, and two-dimensional disturbances not of the similarity form. In a laboratory experiment we might expect the two-dimensional similarity solutions to develop downstream from the channel inlet, and away from the outlet and the sidewalls. Numerical investigations of the full steady two-dimensional

Navier–Stokes equations for flow in a symmetric porous-walled channel of finite length have been carried out by Brady & Acrivos (1981) and Raithby & Knudsen (1974). Brady & Acrivos find that the Berman similarity solution develops downstream of the inlet, but that the fraction of the channel's length over which it holds decreases as R increases. When R is greater than about 6, the similarity solution does not develop at all. However, we should be cautious in interpreting this as implying that the similarity solution is invalid for R greater than 6, for they assume their two-dimensional solutions to be symmetric, and their numerical code effectively solves a time-dependent problem. Recall that at $R = R_1 \approx 6.001353$ the symmetric similarity solution becomes temporally unstable (in a pitchfork bifurcation). It is not then surprising that Brady & Acrivos fail to find a symmetric similarity solution for R greater than about 6. In such full two-dimensional integrations to date, asymmetric solutions of the symmetric problem have not been sought (the integrations have been across half the channel width, with the symmetry condition $\partial u/\partial y = v = 0$ applied on the centreline of the channel). Nor has the asymmetric problem been examined. Unsteady two-dimensional flows in a porous-walled channel, too, await investigation. All would yield interesting information, and indicate the range of wall-suction rates for which the similarity solutions form a good approximation to realizable channel flows.

Laboratory experiments on porous-walled channel flow (Raithby & Knudsen 1974) and of porous-walled pipe flow (Bundy & Weissberg 1970) indicate that the similarity solution develops rapidly away from the inlet when there is fluid injection. The conclusions for suction are less clear cut: a further careful study would be illuminating.

We have described numerical solutions of the ODE governing steady solutions of the Berman problem, and from our numerical results we have inferred the bifurcations which occur. These were summarized in figure 5.

For the time-dependent problem, the limit-cycle solution which holds for large R, when $\epsilon = 1$, has an explosive phase of essentially inviscid growth. For all R, this inviscid *intermediate asymptotic* phase has a finite-time singularity, which does not occur in the full solution of the Proudman–Johnson equation. Instead the inviscid phase seems always to be moderated by viscosity near one wall – the inviscid velocity profile spreads out as time advances, and eventually ceases to represent the full solution accurately when a hump 'hits' the lower wall. The issue of whether solutions of the Proudman–Johnson PDE (6) can develop singularities in a finite time, however, has not been satisfactorily resolved. Our experience is that the numerical overflow which often occurs when integrating this PDE can always be removed by refining the spatial grid, and therefore it does not represent a mathematical singularity in the exact solutions. The numerical overflow which was reported by Childress *et al.* (1989) for the Proudman–Johnson equation with homogeneous boundary conditions was originally interpreted as evidence of a mathematical singularity. Subsequent numerical integrations (S. Childress, personal communication) have shown that a finer spatial grid can always remove the overflow, as in the Berman problem. That is, the numerical overflow does not in fact represent a mathematical singularity. Whether there may yet be such singularities for larger values of the Reynolds number than those tried so far is an open question. An example of a nonlinear PDE which has such 'self-focusing' singularities is the nonlinear Schrödinger equation (Tabor 1989). For other, dissipative PDEs such as the Kuramoto–Sivashinsky equation (Foias *et al.* 1988) and the complex Ginzburg–Landau equation (Doering *et al.* 1988) it has been possible to calculate rigorous bounds on solutions, and it may be possible to apply these techniques to the Proudman–Johnson equation.

An interpretation of the large-R limit cycle for laboratory flows would be premature since we do not know whether the similarity solutions develop in real channels at such high wall-suction rates. In particular, we do not know whether the time-dependent similarity solutions will develop in a realistic flow. A similar comment limits our interpretation of the transition to chaos (§6). Regardless of this limitation, however, the route to chaos is important because it shows a 'Lorenz-like' transition in the full Navier–Stokes equations, and not merely in some low-order truncation. There is a richer structure to the time-dependent solutions of the Berman problem when the walls are accelerating symmetrically (Watson *et al.* 1990) rather than porous. In that case, however, the robustness of the chaos to symmetry breaking is unknown. (We should mention here a related study by Goldshtik & Javorsky (1989) of the similarity solution for the axisymmetric flow between a porous rotating disk and a plane. The Navier–Stokes equations are reduced to a pair of coupled PDEs for the velocities, and a transition to chaos is reported as the suction rate through the porous disk is increased. An analogy with the Lorenz system is made, although the analogy is metaphorical rather than direct because their system is not 'Lorenz-like' in the sense of Glendinning (1987).)

The transition to chaos in the Berman problem is predicted by the theory of dynamical systems to be smooth when the symmetry of the problem is broken, although our numerical calculations indicate that the system must be extremely close to symmetry for complicated dynamics to arise at all from the perturbed homoclinic explosion. This route to chaos in the Navier–Stokes equations may thus be doubly unobservable in practice: first, the similarity solutions may not be stable to three-dimensional disturbances at sufficiently high wall-suction rates; and secondly, it is unlikely that the system could be made sufficiently symmetrical for complicated dynamics. Of course, other asymmetries (or more general experimental imperfections, for example time-dependence or spatial non-uniformity in the suction at the walls) may act to reinforce the chaos. This is an open question.

This work was carried out as part of my Ph.D. research, with funding from the SERC. I am grateful to my Ph.D. supervisor, Professor P. G. Drazin, for much advice and encouragement while this work was in progress. Also to Drs W. H. H. Banks and M. B. Zaturska, in particular for access to their numerical calculations and for discussions on the large-R asymptotics, and to Dr P. Glendinning, who helped me understand the transition to chaos. I would like to thank Dr S. Childress for helpful discussions about the problem of blow-up. The revisions to this manuscript were made with the support of the Air Force Office of Scientific Research grant AFOSR-89-0226 in the Sibley School of Mechanical and Aerospace Engineering at Cornell University.

REFERENCES

AFRAIMOVICH, V. S. & SHIL'NIKOV, L. P. 1983 Strange attractors and quasiattractors. In *Nonlinear Dynamics and Turbulence* (ed. G. I. Barenblatt, G. Iooss & D. D. Pitman), pp. 1–34.

BARENBLATT, G. I. & ZEL'DOVICH, YA. B. 1972 Self-similar solutions as intermediate asymptotics. *Ann. Rev. Fluid Mech.* **4**, 285–312.

BATCHELOR, G. K. 1967 *An Introduction to Fluid Dynamics.* Cambridge University Press.

BERMAN, A. S. 1953 Laminar flow in channels with porous walls. *J. Appl. Phys.* **24**, 1232–1235.

BERZINS, M. & DEW, P. M. 1990 Chebyshev polynomial software for elliptic-parabolic systems of PDEs. *ACM Trans. Math. Software* (to be published).

BRADY, J. F. 1984 Flow development in a porous channel and tube. *Phys. Fluids* **27**, 1061–1067.

BRADY, J. F. & ACRIVOS, A. 1981 Steady flow in a channel or tube with an accelerating surface velocity. An exact solution to the Navier–Stokes equations with reverse flow. *J. Fluid Mech.* **112**, 127–150.

BRADY, J. F. & ACRIVOS, A. 1982 Closed-cavity laminar flows at moderate Reynolds number. *J. Fluid Mech.* **115**, 427–442.

BUNDY, R. D. & WEISSBERG, H. L. 1970 Experimental study of fully developed laminar flow in a porous pipe with wall injection. *Phys. Fluids* **13**, 2613–2615.

CALOGERO, F. 1984 A solvable nonlinear wave equation. *Stud. Appl. Maths* **70**, 189–199.

CHILDRESS, S., IERLEY, G. R., SPIEGEL, E. A. & YOUNG, W. R. 1989 Blow-up of unsteady two-dimensional Euler and Navier–Stokes solutions having stagnation-point form. *J. Fluid Mech.* **203**, 1–22.

COX, S. M. 1989 A similarity solution of the Navier–Stokes equations for two-dimensional flow in a porous-walled channel. Ph.D. thesis, University of Bristol.

COX, S. M. 1990 The transition to chaos in an asymmetric perturbation of the Lorenz system. *Phys. Lett.* A **144**, 325–328.

COX, S. M. 1991 Analysis of steady flow in a channel with one porous wall, or with accelerating walls. *SIAM J. Appl. Maths* (in press).

DOERING, C. R., GIBBON, J. D., HOLM, D. D. & NICOLAENKO, B. 1988 Low-dimensional behaviour in the complex Ginzburg–Landau equation. *Nonlinearity* **1**, 279–309.

DURLOFSKY, L. & BRADY, J. F. 1984 The spatial stability of a class of similarity solutions. *Phys. Fluids* **27**, 1068–1076.

FOIAS, C., NICOLAENKO, B., SELL, G. R. & TEMAM, R. 1988 Inertial manifolds for the Kuramoto–Sivashinsky equation and an estimate of their lowest dimension. *J. Maths Pures Appl.* **67**, 197–226.

GLENDINNING, P. 1987 Asymmetric perturbations of Lorenz-like equations. *Dyn. Stability Systems* **2**, 43–53.

GLENDINNING, P. & SPARROW, C. 1984 Local and global behavior near homoclinic orbits. *J. Statist. Phys.* **35**, 645–696.

GOLDSHTIK, M. A. & JAVORSKY, N. I. 1989 On the flow between a porous rotating disk and a plane. *J. Fluid Mech.* **207**, 1–28.

GUCKENHEIMER, J. & HOLMES, P. 1986 *Nonlinear Oscillations, Dynamical Systems, and Bifurcations of Vector Fields.* Springer.

LORENZ, E. N. 1963 Deterministic nonperiodic flow. *J. Atmos. Sci.* **20**, 130–141.

PROUDMAN, I. 1960 An example of steady laminar flow at large Reynolds number. *J. Fluid Mech.* **9**, 593–602.

PROUDMAN, I. & JOHNSON, K. 1962 Boundary-layer growth near a rear stagnation point. *J. Fluid Mech.* **12**, 161–168.

RAITHBY, G. D. & KNUDSEN, D. C. 1974 Hydrodynamic development in a duct with suction and blowing. *Trans. ASME* E: *J. Appl. Mech.* **41**, 896–902.

ROBINSON, W. A. 1976 The existence of multiple solutions for the laminar flow in a uniformly porous channel with suction at both walls. *J. Engng Maths* **10**, 23–40.

SHRESTHA, G. M. 1967 Singular perturbation problems of laminar flow in a uniformly porous channel in the presence of a transverse magnetic field. *Q. J. Mech. Appl. Maths* **20**, 233–246.

SHRESTHA, G. M. & TERRILL, R. M. 1968 Laminar flow with large injection through parallel and uniformly porous walls of different permeability. *Q. J. Mech. Appl. Maths* **21**, 414–432.

SKALAK, F. M., WANG, C.-Y. 1978 On the nonunique solutions of laminar flow through a porous tube or channel. *SIAM J. Appl. Maths* **34**, 535–544.

SPARROW, C. 1982 *The Lorenz Equations: Bifurcations, Chaos, and Strange Attractors.* Springer.

STUART, J. T. 1988 Euler partial differential equations: singularities in their solution. In *Symposium to Honor Professor C. C. Lin* (ed. D. J. Benney, F. H. Shu & C. Yuan). World Scientific.

TABOR, M. 1989 *Chaos and Integrability in Nonlinear Dynamics. An Introduction.* Wiley.

TERRILL, R. M. 1964 Laminar flow in a uniformly porous channel. *Aeronaut. Q.* **15**, 299–310.

TERRILL, R. M. 1965 Laminar flow in a uniformly porous channel with large injection. *Aeronaut. Q.* **16**, 323–332.

TERRILL, R. M. 1967 Flow through a porous annulus. *Appl. Sci. Res.* **17**, 204–222.

TERRILL, R. M. & SHRESTHA, G. M. 1964 Laminar flow through channels with porous walls and with an applied transverse magnetic field. *Appl. Sci. Res.* **11**, 134–144.

TERRILL, R. M. & SHRESTHA, G. M. 1965 Laminar flow through parallel and uniformly porous walls of different permeability. *Z. Angew. Math. Phys.* **16**, 470–482.

WATSON, E. B. B., BANKS, W. H. H., ZATURSKA, M. B. & DRAZIN, P. G. 1990 On transition to chaos in two-dimensional channel flow symmetrically driven by accelerating walls. *J. Fluid Mech.* **212**, 451–485.

ZATURSKA, M. B., DRAZIN, P. G. & BANKS, W. H. H. 1988 On the flow of a viscous fluid driven along a channel by suction at porous walls. *Fluid Dyn. Res.* **4**, 151–178.